Clim. Past Discuss., 9, 837–890, 2013
www.clim-past-discuss.net/9/837/2013/
doi:10.5194/cpd-9-837-2013

Climate of the Past Discussions
Open Access

Global and regional sea surface temperature trends during Marine Isotope Stage 11

Y. Milker[1,2,*], R. Rachmayani[2], M. Weinkauf[1,2], M. Prange[2], M. Raitzsch[3], M. Schulz[2], and M. Kučera[1,2]

[1]Department of Geosciences, University of Tübingen, Hölderlinstraße 12, 72074 Tübingen, Germany
[2]MARUM – Center for Marine Environmental Sciences and Faculty of Geosciences, University of Bremen, Klagenfurter Straße, 28359 Bremen, Germany
[3]Alfred Wegener Institute for Polar and Marine Research, Am Handelshafen 12, 27570 Bremerhaven, Germany
[*]now at: Geological-Paleontological Institute and Museum, University of Hamburg, Bundesstraße 55, 20146 Hamburg, Germany

Received: 9 January 2013 – Accepted: 4 February 2013 – Published: 12 February 2013

Correspondence to: Y. Milker (yvonne.milker@uni-hamburg.de)

Published by Copernicus Publications on behalf of the European Geosciences Union.

Abstract

The Marine Isotope Stage (MIS) 11 (424–374 ka) was characterized by a protracted deglaciation and an unusually long climatic optimum. It remains unclear to what degree the climate development during this interglacial reflects the unusually weak orbital forcing or greenhouse gas trends. Previously, arguments about the duration and timing of the MIS11 climatic optimum and about the pace of the deglacial warming were based on a small number of key records, which appear to show regional differences. In order to obtain a global signal of climate evolution during MIS11, we compiled a database of 78 sea surface temperature (SST) records from 57 sites spanning MIS11, aligned these individually on the basis of benthic ($N = 28$) or planktonic ($N = 31$) stable oxygen isotope curves to a common time-frame and subjected 48 of them to an Empirical Orthogonal Function (EOF) analysis. The analysis revealed a high commonality among all records, with the principal SST trend explaining almost 49 % of the variability. This trend indicates that on the global scale, the surface ocean underwent rapid deglacial warming during Termination V, in pace with carbon dioxide rise, followed by a broad SST optimum centered at ~ 410 kyr. The second EOF, which explained 19 % of the variability, revealed the existence of a different SST trend, characterized by a delayed onset of the temperature optimum during MIS11 at ~ 398 kyr, followed by a prolonged warm period lasting beyond 380 kyr. This trend is most consistently manifested in the mid-latitude North Atlantic and Mediterranean Sea and is here attributed to the strength of the Atlantic meridional overturning circulation. A sensitivity analysis indicates that these results are robust to record selection and to age-model uncertainties of up to 3–6 kyr, but more sensitive to SST seasonal attribution and SST uncertainties $> 1\,^{\circ}$C. In order to assess the effect of orbital forcing on MIS11 SST trends, the annual and seasonal SST anomalies recorded in a total of 74 proxy records were compared with CCSM3 (Community Climate System Model, version 3) runs for three time slices representing orbital configuration extremes during the peak interglacial of MIS11. The modeled SST anomalies are characterized by a significantly lower variance compared

CPD
9, 837–890, 2013

to the reconstructions. Nevertheless, significant correlations between proxy and model data are found in comparisons on the seasonal basis, indicating that the model captures part of the long-term variability induced by astronomical forcing, which appears to have left a detectable signature in SST trends.

1 Introduction

Marine Isotope stage (MIS) 11 (424–374 ka) (Lisiecki and Raymo, 2005) stands out among the middle Pleistocene interglacials by its unusually long climatic optimum and a subdued orbital forcing due to low orbital eccentricity (Tzedakis et al., 2009). The MIS11 configuration of orbital parameters is similar to the Holocene and MIS11 has been often considered an analogue to the present interglaciation (Berger and Loutre, 1991; Loutre and Berger, 2003; EPICA community members, 2004). However, whereas the present interglaciation has so far lasted through one single summer insolation maximum at 65° N, the MIS11 interglacial optimum spans two such insolation maxima. Further, the deglaciation culminating in MIS11 climatic optimum (Termination V) was associated with an unusually weak orbital forcing, making orbital alignment with the Holocene difficult, and driving a protracted deglacial sea-level rise during Termination V, twice as long as during Termination I (Lisiecki and Raymo, 2005; Rohling et al., 2010; Tzedakis, 2010). In contrast to the differences in orbital parameters, the greenhouse gas concentrations in the atmosphere during MIS11 and the rate of their increase during Termination V were similar when compared to the preindustrial Holocene (Petit et al., 1999; Siegenthaler et al., 2005).

During MIS11, warm interglacial conditions lasted longer than in any other mid to late Pleistocene interglacial and the peak sea level appears to have been slightly higher than at present (Raymo and Mitrovica, 2012). The presence of an extended "climatic optimum", lasting around 30 kyr, has been documented in sea surface temperature records across the world ocean (McManus et al., 1999; Hodell et al., 2000; Kandiano and Bauch, 2003; De Abreu et al., 2005; Voelker et al., 2010; Dickson et al.,

CPD
9, 837–890, 2013

2009; Stein et al., 2009), in temperature proxies from Antarctic ice cores (Petit et al., 1999; Jouzel et al., 2007; Pol et al., 2011) and in terrestrial pollen records (Tzedakis, 2010). Like the Holocene, the MIS11 climatic optimum appears to have been a stable interglacial period (McManus et al., 1999; Oppo et al., 1998), characterized by low-amplitude millennial-scale climate variability (Oppo et al., 1998, 2003; Healey and Thunell, 2004; Pol et al., 2011).

On the other hand, temperatures in the northern high latitudes during MIS11 appear lower than in the Holocene (Bauch et al., 2000; Helmke et al., 2003) and their temporal development seems to deviate from the global trend (Kandiano et al., 2012). These differences have been linked to changes in the strength of the Atlantic meridional overturning circulation, underlining the importance of the response of oceanic circulation to global forcing during Termination V and MIS11 (Dickson et al., 2009). Until now, the congruence of SST trends during MIS11 has never been assessed objectively, on a global basis and with an explicit consideration of dating uncertainty. Such analysis is essential to determine the robustness and timing of MIS11 climatic optimum and the relationship between MIS11 SST trends with global forcing.

Here, we present a global compilation of sea surface temperature (SST) records for MIS11, aligned by oxygen-isotope stratigraphy, that cover a large proportion of the global oceans on both hemispheres. The aim of this study is to analyze temporal trends in the SST records and to investigate their linkage to global and regional climate variability during this period. Specifically, the following questions will be addressed: (i) what are the roles of orbital and greenhouse gas forcing in MIS11 climate variability, (ii) to which extent is regional climate variability reflected in SST trends, (iii) how does tempo-spatial climate variability simulated by a state-of-the-art climate model for orbital configuration extremes of MIS11 correspond to that found in proxy records?

CPD
9, 837–890, 2013

2 Material and methods

2.1 Material

We compiled a total of 78 marine SST records from 57 sites, covering a large geographical range (175° E–172° W and 57° N to 54° S), and water depths from 826 to 4620 m (Table 1). Most records stem from cores drilled in the Atlantic and Pacific Oceans, but the database also includes records from the Indian Ocean, the Southern Ocean, and the Mediterranean Sea (Fig. 1). We have only chosen SST records for which stable benthic or planktonic foraminiferal oxygen isotope data are available with a sufficient temporal resolution to establish a robust stratigraphic framework for each record (Sect. 2.2). Most datasets were derived from the Pangaea (http://www.pangaea.de) and National Oceanic and Atmospheric Administration (NOAA) (ftp://ftp.ncdc.noaa.gov) websites. Data not available online were provided by the principal investigators or extracted from published figures through digital image processing.

The SST records are based on different proxies. Aware of the significant differences in the part of the seasonal SST cycle that is represented by each proxy, we have attributed the individual SST records to seasons. Thus a total of seven records based on planktonic foraminiferal Mg/Ca in low- to mid-latitudes were attributed to annual SST (see Barker et al., 2005), and all 25 alkenone ($U^{k'}_{37}$) records were attributed to annual SST (see Müller et al., 1998) (Fig. 3d). A total of 27 seasonal SST records are based on foraminiferal, radiolarian and diatom assemblages using transfer functions including the Modern Analog Technique (MAT) (Prell, 1985), the Imbrie-Kipp Technique (IKT) (Imbrie and Kipp, 1971), the Revised Analog Method (RAM) (Waelbroeck et al., 1998), and SIMMAX (Pflaumann et al., 1996), while one record based on the artificial neural network approach (Malmgren and Nordlund, 1997; Malmgren et al., 2001) was attributed to annual SST (Fig. 3d). Among the individual studies, the calibration datasets and the exact definitions of the seasons vary, but all transfer functions have been calibrated to a representation of "surface" SST and differences due to different

CPD
9, 837–890, 2013

calibration data are unlikely to affect the shape of the SST trends. Finally, one SST record was derived by subtracting the benthic δ^{18}O from the δ^{18}O signal of the planktic foraminifer *Neogloboquadrina pachyderma* (McManus et al., 1999) and another one using the relative abundance of *N. pachyderma* (sinistral) (Vázquez Riveiros et al., 2010). Both of these records are from high-latitude settings and were considered to represent the summer growth season, following the authors of these studies. Furthermore, we included one stack that is based on the mean SSTs calculated from $U^{k'}_{37}$, Mg/Ca, and Tex^{H}_{86} measurements (Caley et al., 2011) and considered to represent annual SST. Thus, all SST records can be taken at first approximation to represent a "surface" signature, which has been attributed seasonally as far as possible. Nevertheless, we acknowledge that a strict direct comparison of the reconstructed SST values will be challenging and, therefore, we only compare trends and anomalies in this study.

2.2 Chronostratigraphy

To allow a direct comparison of SST trends, all records were tuned to the LR04 stack (Lisiecki and Raymo, 2005) on the basis of benthic or planktonic δ^{18}O. The tuning was carried out for the period between 200 to 550 ka using the AnalySeries software (Paillard et al., 1996) (Fig. 2a–c). The longer tuning time interval enabled a better correlation between the LR04 stack and the δ^{18}O data, because it includes more than one glacial–interglacial cycle. For the majority of the records, the δ^{18}O data with their corresponding core depths were tuned to the LR04 stack. For a few records, particularly in the Southern Hemisphere, the original age models were used to guide the tuning to the LR04 stack. Where both benthic and planktonic δ^{18}O data were available, the benthic records were used for tuning with priority. Depending on the temporal resolution of the records, between 6 and 18 tie points were defined for the target time interval 300–500 ka. This interval was selected because it covers the entire MIS11 and the major portion of the preceding and following glacials, allowing multiple robust tie points to be defined. The temporal resolution of all proxy records was calculated for

CPD
9, 837–890, 2013

the 300–500 ka time interval (Fig. 3a, Table 1). Age model quality was evaluated on the basis of the correlation between the LR04 stack and the stable oxygen isotope curve of each record, as implemented in the AnalySeries software (Table 1).

2.3 Analysis of SST trends

To extract principle SST trends in the global compilation, the stratigraphically tuned SST records were subjected to an Empirical Orthogonal Function analysis (principal components analysis applied on equally spaced time series). This method projects a multivariate dataset onto a subset of a few principle components, whilst retaining as much information as possible (Hannachi et al., 2007; Jolliffe, 2002; Hammer and Harper, 2006). As the first step of the EOF analysis, the tuned SST time series were linearly interpolated to a temporal resolution of 1000 yr and all records were normalized to unit variance, preventing the first EOFs from being dominated by variables with large variance. Of the total of 57 sites, SST records from 48 sites (34 representing annual and 14 representing caloric summer SST) covered the interval of 370–430 ka and were included in the analysis (Table 1, Fig. 3e). This interval was selected to allow the inclusion of the most records, whilst covering the entire MIS11. The 11 records not included in the analysis either ended or started within MIS11. Since we were only interested in the shape of SST trends, we have merged records attributed to annual and summer SST in one joint analysis. We believe this is justified since the biggest difference is likely to be that of a systematic offset, rather than a difference in the shape of the trends. Nevertheless, to assess to what degree this decision may have affected the results, we have also carried out the analyses separately for annual and caloric summer SST.

In order to test the EOF sensitivity to age model uncertainty, the analysis was repeated on data in which the age control points of all records were randomly resampled with an age uncertainty of 3, 5, and 6 kyr. The lowest value corresponds to the mean temporal resolution of the records (Table 1); values higher than 6 kyr were not tested as they would equate to age uncertainties approaching the shortest orbital cycle, implying

CPD
9, 837–890, 2013

a total failure of the orbital tuning procedure. All age models in this study are based on the age assignment to a small number of distinct features in stable isotope records, between which an interpolation takes place. As first approximation, we consider that each of the age model control points is liable to the same uncertainty, and that these uncertainties are symmetrical and independent of each other. The randomized age model for each record was then created by stepwise linear correlation between the resampled control points. We have not carried out an auto-correlated age uncertainty propagation between the control points, but the algorithm we used detected and rejected all trials where the resampling created chronological reversals (such situation may arise when age model control points are closer than twice the age uncertainty of the resampling).

Next, in order to assess the robustness of the EOF pattern to uncertainties in the SST values, the SST reconstructions were resampled under a simulated proxy uncertainty of 1, 2, and 4 °C. The lowest value corresponds to the typical value of a SST proxy uncertainty due to calibration. Higher values of SST uncertainty acknowledge the possibility that the SST reconstructions may be misattributed seasonally between glacial and interglacial ocean conditions, reflecting, for example, shifts in the production season of the proxy carrier. Finally, we used a jackknifing approach to examine the sensitivity of the EOFs to the number of records used in the analysis. EOFs were recalculated, with 1000 replications, after randomly excluding 5, 15, 25, and 35 records during each replication. The EOF analysis was then carried out with 1000 replicates considering various combinations of age model uncertainty, SST proxy uncertainty and record exclusion. All EOF calculations were carried out with an algorithm written in MATLAB R2012a, which is available in the Supplement (S3).

2.4 Model-data comparison of climate variability

A comparison of SST anomalies in the proxy data with climate model output was carried out for three time slices (394, 405, and 416 ka before present) during the peak MIS11 interglacial (MIS11.3) when the influence of ice sheets on climate was supposed

CPD
9, 837–890, 2013

to be small. The three time slices reflect different extremes of the orbital configurations during peak MIS11. The 394 and 416 ka time slices are characterized by minimum and maximum obliquity (cf. Fig. 8a), respectively, while precession is almost identical. The 405 ka time slice coincides with the LR04 oxygen isotopic minimum (Lisiecki and Raymo, 2005) and high northern summer insolation (cf. Fig. 8a). For model-data comparison, arithmetic averages of all proxy values in each tuned record that fall into a 10 kyr interval centered on the respective model time slice were extracted from the proxy records. In this way, we have made sure that age model uncertainties in the proxy data were taken into account, whilst we acknowledge that the proxy time-slice data are likely to have been smoothed. The time slice simulations were performed with the National Center for Atmospheric Research (NCAR) Community Climate System Model version 3 (CCSM3) which is described in the following section.

CCSM3 is a state-of-the-art coupled climate model that performs without flux corrections. The global model is composed of four separate components representing atmosphere, ocean, land, and sea ice (Collins et al., 2006). Here, we use the low-resolution version of CCSM3, which is described in detail by Yeager et al. (2006). In this version, the resolution of the atmosphere is given by T31 (3.75° transform grid) spectral truncation with 26 layers, while the ocean model has a nominal horizontal resolution of 3° (like the sea-ice component) with 25 vertical levels. The latitudinal resolution of the ocean grid is variable, with finer resolution around the equator (0.9°). The land model is defined on the same horizontal grid as the atmosphere and includes components for biogeophysics, biogeochemistry, the hydrologic cycle, as well as a dynamic global vegetation model. In order to improve the simulation of vegetation cover, new parameterizations for canopy interception and soil evaporation have been implemented into the land component (Oleson et al., 2008).

A pre-industrial control run was performed following the protocol established by the Paleoclimate Modeling Intercomparison Project, Phase 2 (Braconnot et al., 2007; Otto-Bliesner et al., 2006; Merkel et al., 2010). The control run was integrated for 600 yr starting from present day initial conditions. For the selected time slices of MIS11.3,

CPD
9, 837–890, 2013

appropriate orbital parameters (Berger, 1978) and greenhouse gas concentrations were prescribed, as given in Table 2, while all other forcings (ice sheet configuration, ozone distribution, sulfate aerosols, carbonaceous aerosols, solar constant) were kept at pre-industrial levels. Starting from the last year of the (quasi-)equilibrated pre-industrial control run, all MIS11.3 simulations were integrated for 400 yr so that the surface climatologies could reach a statistical equilibrium. For each experiment, the mean of the last 100 simulation years was used for analysis.

For a direct proxy-model comparison, we used only such proxy SST records for which at least one value was available in each of the three time-slice intervals and calculated the differences between the SST average for the three time slices and the SST average of each time slice. In all cases, the seasonal attribution has been preserved, allowing data-model comparison on a seasonal basis. The comparison is synoptic in that northern summer SST and southern winter SST are analyzed together and vice versa. The eventually selected 74 records contain a total of 35 annual, 16 Northern Hemisphere summer, and 23 Northern Hemisphere winter SST records (Fig. 3f, Table 1). Model data have been extracted from the surface layer (0–20 m) field of the nearest grid cell to each proxy record. For the data-model comparison, we calculated the proxy-based and modeled SST anomalies of the Northern Hemisphere summer (July–September in the model) and winter (January–March in the model) periods and the annual SST anomalies relative to the mean SST of the 390–420 ka time interval (the average of the 394, 405, and 416 ka time slices in the model).

To test the agreement between proxy and modelled SST anomalies in a quantitative way, the correlation between the proxy and modelled data for each season and each time slice was calculated using the PAST software package (Hammer et al., 2001). The type of correlation analyses was adapted to the results of normality tests applied on the data sets. Pearson's product-moment correlation was used where the data were normally distributed (Shapiro–Wilk test), while Spearman's rank-order correlation was used when the data did not meet these requirements. In order to assess not only the strength of the direct relationship between the modelled and proxy-based anomalies,

CPD
9, 837–890, 2013

but also to compare the direction of change in the data, Cohen's κ (Cohen, 1960) was used. Here, the temperature anomaly values were categorized into three nominal values, i.e. negative, positive, and no change relative to the mean SST of the 390–420 ka time interval (the average of the 394, 405, and 416 ka time slices in the model data). On the basis of those categories, it was counted how often proxy data and model predictions were in agreement with each other, and how often they contradicted and if so, in which way they contradicted (e.g. model = positive and proxy = negative, or model = no change and proxy = positive). This resulted in contingency tables with counts of all nine possible relations, from which Cohen's κ and corresponding p-values (for H_0 = no agreement between raters) were calculated in the SPSS software package (version 20). Verbal assignments of quality of agreement solely on the basis of the κ value are in accordance with standard values given in the literature (e.g. Altman, 1991). Finally, to quantify the differences in variability in the proxy records and the climate model, the variance of the SST anomalies in the proxy and model data sets were calculated for each time slice and season, and compared using an F-test.

3 Results

3.1 Age model quality

In order to quantify the quality of our age models, we examined both the correlation of the δ^{18}O records with the LR04 stack (Lisiecki and Raymo, 2005) as well as their temporal resolution. The majority of the benthic isotope records (44 records, i.e. 77 %) shows a high correlation of $r \geq 0.80$ for the entire tuning time interval between ~200 and ~550 ka (Table 1). Ten records (18 %) show a moderate correlation with the LR04 stack ($r = 0.60$ between $r = 0.80$). Three records show a low correlation with the benthic stack with $r = 0.50$ for ODP 882, $r = 0.46$ for MD03-2699, and $r = 0.36$ for ODP 1168. The records from MD03-2699 and ODP 1168 are characterized by low δ^{18}O values in the later part of MIS11. According to Voelker et al. (2007) the benthic δ^{18}O values of

CPD
9, 837–890, 2013

core MD03-2669 are strongly affected by the Mediterranean Outflow Water (MOW) during glacial and interglacial inceptions, making it difficult to establish a benthic-isotope-based age model. We therefore used the LR04 age model provided by Voelker et al. (2010), which is mainly based on the correlation of the benthic δ^{18}O record of MD03-2669 with that of ODP Site 980 (Oppo et al., 1998; McManus et al., 1999). The benthic δ^{18}O record of ODP 1168 was tuned with the help of the original age model given in Nürnberg et al. (2004). The ODP 882 benthic δ^{18}O record has the lowest resolution of all records used and the tuning to the LR04 stack was guided by the age model given in Haug (1995). When only the MIS11 interval (370–430 ka) is considered, 52 records (91 %) show a correlation with the LR04 stack higher than $r = 0.8$. Four records (8 %) exhibit correlation coefficients between $r = 0.6$ and $r = 0.8$ and one record (ODP 1168) has a correlation of less than 0.6 (i.e. $r = 0.19$) (Table 1). To determine the δ^{18}O records' quality, the records were divided into classes depending on their temporal resolution. For records MD97-2142 and MD01-2443 the mean temporal resolution based on two different δ^{18}O records was calculated (Table 1). Eleven records (19.3 %) have a temporal resolution higher than 1000 yr (Fig. 3a). A total of 21 records (36.9 %) have a temporal resolution between 1000 and 3000 yr, and 16 records (28.0 %) have a resolution between 3000 and 5000 years. Nine of the records (15.8 %) have a low temporal resolution of less than 5000 yr (Fig. 3a). The mean temporal resolution of all records used is approximately 3000 yr. This is the value which was used as the minimum estimate of age uncertainty in the age-model sensitivity simulation.

3.2 Temporal resolution of SST proxy records

To evaluate the temporal resolution of SST records, the records have been divided into the same classes as described above for the δ^{18}O records. For records having more than one SST record, the mean temporal SST resolution was calculated for this evaluation. A total of eight SST records (14.0 %) have a temporal resolution of more than 1000 yr (Fig. 3b), 24 records (43.0 %) have a moderate temporal resolution between 1000 and 3000 yr, and 14 records (24.6 %) have a resolution between 3000 and

CPD
9, 837–890, 2013

5000 yr. Eleven SST proxy records (19.3 %) have a low resolution of less than 5000 yr (Fig. 3b). The mean temporal resolution is 3127 yr, indicating that the records should collectively be able to resolve orbital-scale variability, but not millennial variability. Depending on the specific temporal resolution of each record, varying amounts of SST data points were available for the comparison of the proxy with modeled SST anomalies for the 390–420 ka time interval. From a total of 74 records used for this comparison, 26 records (35.1 %) provided only less than ten data points each for the total time interval (Fig. 3c). For 36 records (48.6 %) 10–40 data points per record were available, whereas 9 records (12.1%) contained more than 40 but less than 130 data points per record, and three records (4.1 %) provided more than 130 data points each.

3.3 Empirical Orthogonal Function analysis

EOF analysis (Fig. 4) of the 48 SST records spanning the entire target time interval revealed the existence of a strong commonality in the shape of the SST trends. The first three EOFs together explained around three quarters of the variability in the data, irrespective of the combination of age-model and SST-proxy uncertainty and record selection (Table 3). Almost one half of the variability is explained by the first EOF, which describes a temporal trend of a rapid deglaciation, followed by a broad temperature optimum centered on 410 ka and a slow decrease of SST towards the end of MIS11. The second EOF explains nearly 20 % of the total variability and shows a delayed onset of the temperature optimum during MIS11 after 410 ka, followed by a prolonged warm period lasting beyond 380 ka. The third EOF explains around 8 % of the total variability and shows a cyclic pattern with a period of about 30 kyr.

For the first EOF, 40 % of the records have significant positive loadings >0.75, 33 % of the records have positive loadings between 0.5 and 0.75, and only 4 records (ODP 999, ODP 1168, RC11-210 and V22-174) show negative loadings (Fig. 5). The latter records reflect SST changes in the Mediterranean Sea, the tropical Atlantic and Pacific, as well as in southeastern Australian coastal regions. In contrast, the loadings of the second EOF are more diverse and show a geographical pattern. Only four

CPD
9, 837–890, 2013

of the records show strong positive loadings > 0.75 to EOF2 (Fig. 5). These records are primarily associated with SST changes in the North Atlantic region (IODP U1313, ODP 958) and the Mediterranean Sea (ODP 976). Records with positive loadings to EOF2 between 0.5 and 0.75 are further observed in the Caribbean Sea (V12-122), at the western coast of South Africa (ODP 1082), northwest off Australia (MD00-2361), and in the North Pacific (ODP 882, RC11-210). Finally, high loadings of the third EOF are limited to a few records, indicating that this EOF (and all subsequent EOFs) tends to express patterns specific for individual sites, rather than highlighting commonalities among the records. Specifically, the summer SST variations in one core (GIK 13519) from the tropical Atlantic show significant positive loadings and the summer SST changes in another core (RC 11-210) from the tropical Pacific Ocean show significant negative loadings to EOF3 (Fig. 5).

Both the shape of the first two EOFs (Fig. 4) and the amount of variance explained by them are remarkably robust to age-model and temperature uncertainty (Table 3). The temperature uncertainty has a stronger influence on the EOF robustness than the uncertainty of the age model. Compared with a temperature uncertainty of 1 °C, a temperature uncertainty of 4 °C reduces the variance explained by EOF1 from 48 to 35 % (Table 3). In contrast, an increase of age uncertainty from 3 to 6 kyr reduces the amount of variance explained by the first EOF by less than 1 % (Table 3). Similarly, a reduction of the number of records included in the analysis has a relatively small influence on the variance that is explained by the EOFs, as long as the subsampling is limited to more than 50 % of the total number of records (Table 3). A similar pattern of robustness against uncertainties and subsampling is seen in the scores of the first two EOFs (Fig. 4). The uncertainties (expressed as the 90 % confidence interval) of the score values increase only moderately with an increasing age uncertainty from 3 to 6 kyr, but more rapidly for rising temperature uncertainties.

In contrast to the robustness of the first two EOFs, the third EOF scores are sensitive both with respect to temperature uncertainty and record selection (jackknifing). The cyclic signal of EOF3 loses significance already at temperature uncertainty of 2 °C and

CPD
9, 837–890, 2013

with jackknifing at the level of withholding around 25 records at a time (Fig. 4). This behavior is consistent with the EOF3 signal being associated with a small number of records characterized by low amplitude of the SST signal. We conclude that the third EOF, and by inference all subsequent ones, do not express any general climatic signals and are not interpreted further in this study.

The EOF analyses carried out separately for the 34 annual and 14 summer SST records show similar general trends for the first two components, but small temporal lags with respect to the joint analysis (Fig. S1 in the Supplement). The lags amount to around 3–4 kyr, which coincides with the average temporal resolution of the records. The loadings of individual records in the separate analyses are largely similar to those in the joint analysis (Fig. S2 in the Supplement).

3.4 Comparison of proxy with modeled SST anomalies

The most striking pattern when comparing the proxy-based SST anomalies with model results is the large difference in their variance. Whilst proxy-based SST anomalies range by 4 °C (up to 6 °C), the modeled SST anomalies range irrespective of season or time slice rarely by more than 1 °C. This pattern is clearly seen in the comparison of the variances of the anomalies in proxy data and model results (Table 4). Notwithstanding the striking differences in the amount of SST change at the studied sites between the proxy data and the model, the direction of change and the regional patterns of anomalies show a number of similarities.

A comparison between the proxy-based and modeled SST anomalies in MIS11 (Fig. 6) shows a generally better agreement for the boreal summer than for the boreal winter and the annual temperature anomalies (the latter is not shown). For the boreal summer, a robust trend to colder (390–400 ka) and warmer temperatures (400–410 and 410–420 ka) can be observed for the northernmost Atlantic region (Fig. 6). On the other hand, a higher SST increase in the North Atlantic was modeled for the 410–420 ka time slice, while the proxy records show a higher SST increase for the 400–410 ka time interval. Modeled positive SST anomalies in the (Sub)Tropics during

CPD
9, 837–890, 2013

the 390–400 ka time interval only partly agree with the SST anomalies recorded in the sediments, while negative SST anomalies modeled for the Southern Ocean region are in better accordance with the proxy data. The general temperature increase simulated for the 400–410 ka time slice is also reflected by the positive SST anomalies in the proxy records except for the tropical Pacific and Indian Oceans. A temperature increase in the Northern Hemisphere accompanied by a temperature decrease in the (Sub)Tropics as reflected by modeled positive and negative SST anomalies, respectively, can also be observed in the proxy data for the 410–420 ka interval, especially for the Atlantic and Indian Oceans and the South China Sea. For the tropical Pacific, the Caribbean Sea, and for two South Atlantic sites the proxy data show opposite trends to the model data (Fig. 6).

The modeled negative SST anomalies in the Southern Hemisphere for the boreal winter season for the 390–400 ka time slice generally agree well with the proxy data, while model and proxy data for the (sub)tropical regions as well as the Northern Hemisphere partly show opposite trends. The simulated SST increase in the Northern Hemisphere and the (Sub)Tropics accompanied by negative anomalies in the Southern Hemisphere during the 400 to 410 ka time interval can also be observed from the proxy data for the Atlantic and Southern Ocean regions, while the observations disagree with the model data for the tropical Pacific and the South China Sea (Fig. 6). Modeled positive SST anomalies in the Southern Hemisphere and negative temperature anomalies in the (Sub)Tropics are in agreement with most of the proxy records of the 410–420 ka interval, too, while particularly in the North Atlantic model and proxy data show opposite trends.

Despite the apparently good qualitative agreement between model and proxy data (Fig. 6), a quantitative comparison shows a different picture (Fig. 7, Table 4). A statistically significant correlation between proxy and model data can be observed for the boreal summer for the 390–400 and 410–420 ka intervals, with $r = 0.56$ ($p = 0.026$) and $r = 0.64$ ($p = 0.008$), respectively, as well as for the boreal winter for the 400–410 ka period ($r = 0.43$, $p = 0.043$). For all other time slices, the seasonal and annual SST

CPD
9, 837–890, 2013

anomalies show low correlations between proxy and modeled data (Table 4, Fig. 7). Cohen's κ, which was used to test whether or not the proxy and modeled data are qualitatively in agreement, shows a fair agreement for boreal summer during the 390–400 and 410–420 ka time slices as well as for the boreal winter during the 400–410 and 410–420 ka time intervals (Table 4). However, all these agreements are not statistically significant, with p-values ranging between 0.091 and 0.932.

4 Discussion

4.1 Global and regional climate trends in the proxy SST records

Under the limitation of the uncertainty in the alignment of the benthic oxygen isotope stack with insolation as carried out by Lisiecki and Raymo (2005), it is possible to explore the relationship between insolation forcing and the global SST pattern during MIS11 as revealed by the EOF1 scores (Fig. 8a). Such comparison is justified, because the SST records at each site are co-registered with the stable oxygen isotope variations used to align the records temporarily, but are in all cases entirely independent of these. This comparison reveals a rapid global temperature rise during Termination V occurring between 430 and 425 kyr. Highest global temperatures during MIS11 were reached at around 411 kyr when the high latitude summer insolation was at its minimum. The SST cooling trend into the glacial inception started at around 405 kyr, corresponding to the onset of ice-sheet growth as indicated by benthic isotopes and the Red Sea sea-level curve (Fig. 8d).

Across MIS11, the first EOF1 follows a consistent glacial-interglacial pattern with cold SSTs during MIS12 (> 430 ka) and MIS10 (< 370 ka), and a relatively long duration of warmer SSTs from 416 to 405 kyr. A similar trend is reflected in the Antarctic temperature change based on the deuterium record of the EPICA Dome C ice core (Jouzel et al., 2007) (Figs. 8b and 9b). However, the position of the interglacial temperature peak is offset with a temperature peak in the Antarctic record lagging the EOF1 signal as well

CPD
9, 837–890, 2013

as the mean global temperature peak calculated from all records (not shown here) by ~4 kyr (Figs. 8b and 10). The EOF1 signal is similar to mean relative SST changes in the South Atlantic and the Southern Ocean (Fig. 8b), while North Atlantic records with high loadings to EOF1 are characterized by a slower temperature decrease during the late MIS11 period – a pattern more similar to the CO_2 record measured in the Dome C Antarctic ice core (Siegenthaler et al., 2005) (Figs. 8c and 9a). Compared to the $\delta^{18}O$ sea-water record of ODP Hole 1123 as a proxy for ice volume (Elderfield et al., 2012), it seems that the deglacial SST rise indicated by EOF1 preceded the reduction of the global ice volume by ~5 kyr (Fig. 8d and e). This pattern remains even when the sea level development during MIS11 is approximated by the Lisiecki and Raymo (2005) stack or by the Red Sea stable isotope record by Rohling et al. (2009) (Figs. 8d, 9c and d),indicating a faster reaction of the surface ocean to insolation and greenhouse gas forcing than that of the slowly melting ice sheets.

The temporal resolution of our study and the level of temporal uncertainty make it difficult to address the phasing of different proxies during MIS11 at millennial time scales, but we note that the global SST trend indicated by EOF1 scores does not precede CO_2 (Fig. 8c). Further, we observe a lag between the global SST peak and the temperature peak over Antarctica (Fig. 8b). This lag is around 4 kyr and is robust to dating uncertainties (Fig. 10). This would indicate that during the interglacial, temperature over Antarctica was not as closely coupled to the global mean as during the deglaciation, perhaps reflecting more strongly the antiphased Southern Hemisphere insolation pattern (Laepple et al., 2011).

The second EOF scores in our analysis follow a trend that differs from the global pattern and indicate a later establishment of a relative temperature maximum and a longer-lasting period of warmer temperatures during late MIS11 and into MIS10 (Fig. 8e and f). This regional trend is primarily reflected in the SST records of the mid-latitude North Atlantic, the Mediterranean Sea as well as in one record south off Australia, where high positive loadings to EOF2 are observed (Fig. 5). A similar trend, with delayed onset of interglacial conditions after Termination V and a longer lasting interglacial optimum, has

CPD
9, 837–890, 2013

been recently reported also from the Eastern Mediterranean (Maiorano et al., 2012). The apparent later onset of MIS11 optimum and the longer duration of interglacial warmth have been also noted by the authors of the individual records included in our compilation, particularly for records from the North Atlantic region. These authors hypothesized that the persistence of the northern ice sheets throughout MIS11 may have led to a dominant negative mode of the North Atlantic Oscillation (NAO) (Kandiano et al., 2012) whilst the associated sustained meltwater input in the (sub-)polar regions may have resulted in a less stable AMOC (Voelker et al., 2010). In either case, these phenomena would lead to a reduced ocean heat transfer into the North Atlantic, causing a delayed optimum in the SST trends. Indeed, Dickson et al. (2009) conclude that a stronger AMOC during MIS11 was first established at 415 ka. Similarly, mean $\delta^{13}C$ of benthic foraminifera from water depths between 1100 and 2300 m in the North Atlantic that can be used as a proxy for NADW production Lisiecki et al. (2008) show increasing values from 425 to 405 ka, where the heaviest values were reached before only slightly decreasing until the end of MIS11 (Fig. 8f). This trend, which is indicative for enhanced NADW production between 410 and 400 ka, is quite similar to our EOF2 scores as well as to the mean relative temperature anomaly trends found in the records with high EOF2 loadings (Fig. 8e and f). The persistence of longer lasting warmer temperatures in the terrestrial high northern latitudes in the late MIS11 and into MIS10 has also been explained by a weaker Siberian High pressure system during times of insolation minima due to lower ice and snow accumulation rates, leading to weakened East Asian winter monsoon (EAWM) as reflected by the GT32 grain size distribution in Chinese loess sequences (Hao et al., 2012) showing a similar pattern to our EOF2 signal (Fig. 8f).

4.2 Comparison of the climate variability between proxy and model SST

The observation of a much lower variance in modeled temperature trends when compared to paleo-data (Table 4) has been found in other studies where marine and terrestrial proxy have been compared with simulated temperature trends for the Holocene

CPD
9, 837–890, 2013

period (Brewer et al., 2007; Sundqvist et al., 2010; Zhang et al., 2010; O'ishi and Abe-Ouchi, 2011; Lohmann et al., 2012). In principle, such disagreement might be caused by an underestimation of temperature changes in climate models, as also suggested by e.g. O'ishi and Abe-Ouchi (2011), Lohmann et al. (2012) and Brewer et al. (2007), by an overestimated proxy SST variability, or a combination of both. Underestimation of climate variability in model simulations may be caused by shortcomings in the model physics (e.g. subgrid-scale parameterizations associated with clouds in the atmosphere or mixing in the ocean) and/or missing climate components (e.g. continental ice sheets) resulting in a lack of potentially important feedback mechanisms. At single sites, undersimulated SST variance may also be caused by too coarse grid resolution, such that e.g. shifts in oceanic fronts or upwelling zones are not resolved. Higher variance in the proxy data may result from noise and calibration uncertainties in the proxy records as also suggested by Brewer et al. (2007) and Sundqvist et al. (2010) as well as from a different temporal SST resolution. The latter phenomenon, however, should lead to a lowering of proxy variance with record resolution (assuming that the records are all subsampling a signal with similar spectral properties).

In order to explore the potential causes of variance in the SST reconstructions by proxies, we plot SST variance against sampling resolution for all records using the proxy-model comparison (Fig. 11). The majority (eight) of the SST records with higher variability (Fig. 11) was reconstructed with the Modern Analog Technique (MAT) and other transfer functions applied on microfossils such as radiolarians, diatoms and foraminifera. The main assumptions when using microfossils for past SST estimates via transfer functions are that (1) the microfossil composition that is used to create a transfer function is systematically related to SST and (2) the ecology of the microfossil assemblages has not significantly changed since the time of interest. The presence of a variable SST during the MIS11 indicated by these methods thus could reflect the effects of nuisance parameters of the reconstructed SST or large shifts in the ecology of the microfossils. The latter seems unlikely on the time scale of one glacial cycle, but the former could indeed be significant, especially where the fossil assemblages differed

CPD
9, 837–890, 2013

from the calibration dataset, resulting in the detection of very different modern analogs with small changes in the assemblages. On the other hand, regression based transfer function methods, such as the MAT and the Imbrie-Kipp method, are unlikely to yield SST reconstructions with variance inflating the level of variance in the assemblage data. In our case, SST records based on MAT yield for records with similar resolution similar variance (Fig. 11), indicating that the variance of the reconstructions is unlikely to have been inflated due to the presence of no-analog faunas. In individual cases, the high variance in SST reconstructions by proxies can be attributed to nuisance variables. For example, Becquey and Gersonde (2002) concluded that carbonate dissolution may result in an over- or underestimation of SSTs when using foraminifera with varying dissolution resistance for the application of transfer functions. These authors further conclude that their summer SSTs estimated with MAT for core PS2489 (used in this study) are overestimated by 6–7 °C for a short interval within MIS11. Whether or not the same can be said for all records in this study remains unclear.

Despite the large differences in variance and considering all the potential sources of uncertainty in the proxy-based SST values, it is remarkable that in several cases not only a visual agreement between the direction of SST change implied by data and models is similar, but also a positive relationship between the values of SST anomalies from both approaches can be observed (Figs. 6 and 7). Whereas it is likely that many of the proxies used could produce SST reconstructions systematically shifted from their a-priori seasonal or vertical attribution, the calculation of SST anomalies between the investigated time slices should largely reduce this problem, as long as the shifts in species ecology causing such misattribution remained temporarily stable. Apparently, especially for the boreal summer season reconstructions, the signal in the proxy-based SST anomalies resonated with processes captured by the CCSM3 model runs. Since these model runs differ mainly by orbital parameters (with greenhouse gas concentrations being largely similar, Table 2), it appears that orbital forcing has left a detectable signature in the global SST pattern during MIS11, despite its unusually low magnitude.

CPD
9, 837–890, 2013

5 Conclusions

Using a compilation of SST records from 57 sites, aligned to a common time scale through oxygen isotope stratigraphy, and a series of CCSM3 model runs forced by greenhouse gas concentrations and orbital parameters, we investigated global patterns of MIS11 SST and their correlation with forcing mechanisms.

- An empirical orthogonal function analysis of 48 SST records revealed the presence of two main SST trends, which collectively explained nearly three quarters of the variation in the dataset. We have shown that the results of this analysis are robust against sample selection and errors in the age model, but are more sensitive to SST uncertainty.
- The main SST trend describes the global glacial-interglacial pattern, showing rapid deglaciation followed by a broad climatic optimum culminating around 410 ka. The SST development during MIS11 optimum is not in phase with Antarctic temperature and CO_2. This lag is the dominant signal in the second EOF. We speculate that this phase difference, which is most strongly manifested in the North Atlantic, may be explained by a later establishment of a stable AMOC in MIS11.
- The second EOF further differs from the global SST trend by a protracted warmer period during MIS11, lasting into MIS10. This regional trend may reflect not only a later onset but also a longer duration of a stable North Atlantic THC during MIS11.
- The comparison of the CCSM3 model with the proxy data shows that similar temperature trends can be found especially for the summer seasons. It further shows that the SST variability found in the proxy data is significantly higher than in the model. This is more likely a consequence of an underestimation of SST changes in climate models. Alternatively, SST reconstructions for MIS11 would have to be subject to pervasive influence of nuisance parameters which vary at millennial

CPD
9, 837–890, 2013

time scales. The general agreement between proxy-derived and modeled SST anomalies indicates the MIS11 climate was responding to insolation forcing, despite the low orbital eccentricity.

Supplementary material related to this article is available online at: http://www.clim-past-discuss.net/9/837/2013/cpd-9-837-2013-supplement.zip.

Acknowledgements. We are grateful to the following colleagues for providing their datasets: T. Bickert, K. Billups, P. De Deckker, P. Dekens, H. Elderfield, J. M. Gonzales Donoso, B. W. Hayward, C. Hillaire-Marcel, E. Kandiano, K. Lawrence, D. Lea, L. T. Li, D. Nürnberg, F. Peeters, C. Pelejero, M.-S. Poli, S. Sepulcre, K.-J. Wei, J. Cheng, and M. Ziegler. We further thank A. Govin for her helpful comments. The study was funded by the Deutsche Forschungsgemeinschaft (DFG) through the Priority Programme "INTERDYNAMIC". CCSM3 simulations were performed on the SGI Altix supercomputer of the Norddeutscher Verbund für Hoch- und Höchstleistungsrechnen (HLRN). The presented data used for EOF analyses and the CCSM3 model data will be available at the PANGAEA data base (www.pangaea.de).

References

Altman, D. G.: Practical Statistics for Medical Research, CRC Texts in Statistical Science, Chapman & Hall, Boca Raton, 1991.

Bard, E. and Rickaby, R. E. M.: Migration of the subtropical front as a modulator of glacial climate, Nature, 460, 380–384, 2009.

Barker, S., Cacho, I., Benwayc, H., and Tachikawa, K.: Planktonic foraminiferal Mg/Ca as a proxy for past oceanic temperatures: a methodological overview and data compilation for the Last Glacial Maximum, Quaternary Sci. Rev., 24, 821–834, 2005.

Bauch, H. A., Erlenkeuser, H., Helmke, J. P., and Struck, U.: A paleoclimatic evaluation of marine oxygen isotope stage 11 in the high-northern Atlantic (Nordic seas), Global Planet. Change, 24, 27–39, 2000.

Becquey, S. and Gersonde, R.: Past hydrographic and climatic changes in the Subantarctic Zone of the South Atlantic – The Pleistocene record from ODP Site 1090, Palaeogeogr. Palaeoecl., 182, 221–239, 2002.
Becquey, S. and Gersonde, R.: A 0.55-Ma paleotemperature record from the Subantarctic zone: Implications for Antarctic Circumpolar Current development, Paleoceanography, 18, 1014, doi:10.1029/2000PA000576, 2003.
Berger, A.: Long-term variations of daily insolation and Quaternary climatic changes, J. Atmos. Sci., 35, 2362–2367, 1978.
Berger, A. and Loutre, M. F.: Insolation values for the climate of the last 10 million years, Quaternary Sci. Rev., 10, 297–317, 1991.
Braconnot, P., Otto-Bliesner, B., Harrison, S., Joussaume, S., Peterchmitt, J.-Y., Abe-Ouchi, A., Crucifix, M., Driesschaert, E., Fichefet, Th., Hewitt, C. D., Kageyama, M., Kitoh, A., Loutre, M.-F., Marti, O., Merkel, U., Ramstein, G., Valdes, P., Weber, L., Yu, Y., and Zhao, Y.: Results of PMIP2 coupled simulations of the Mid-Holocene and Last Glacial Maximum – Part 2: feedbacks with emphasis on the location of the ITCZ and mid- and high latitudes heat budget, Clim. Past, 3, 279–296, doi:10.5194/cp-3-279-2007, 2007.
Brewer, S., Guiot, J., and Torre, F.: Mid-Holocene climate change in Europe: a data-model comparison, Clim. Past, 3, 499–512, doi:10.5194/cp-3-499-2007, 2007.
Caley, T., Kim, J.-H., Malaizë, B., Giraudeau, J., Laepple, T., Caillon, N., Charlier, K., Rebaubier, H., Rossignol, L., Castañeda, I. S., Schouten, S., and Sinninghe Damsté, J. S.: High-latitude obliquity as a dominant forcing in the Agulhas current system, Clim. Past, 7, 1285–1296, doi:10.5194/cp-7-1285-2011, 2011.
Chen, M.-T., Chang, Y.-P., Chang, C.-C., Wang, L.-W., Wang, C.-H., and Yu, E.-F.: Late Quaternary sea-surface temperature variations in the southeast Atlantic: a planktic foraminifer faunal record of the past 600 000 yr (IMAGES II MD962085), Mar. Geol., 180, 163–181, 2002.
Chen, M.-T., Shiau, L.-J., Yu, P.-S., Chiu, T.-C., Chen, Y.-G., and Wei, K.-Y.: 500 000-Year records of carbonate, organic carbon, and foraminiferal sea-surface temperature from the southeastern South China Sea (near Palawan Island), Palaeogeogr. Palaeocl., 197, 113–131, 2003.
Clemens, S. C. and Prell, W. J.: Oxygen and carbon isotopes from Site 1146, northern South China Sea, Proc. ODP, Sci. Results, 184, 1–8, 2003.

CPD
9, 837–890, 2013

Clemens, S. C., Murray, D. W., and Prell, W. J.: Nonstationary phase of the Plio-Pleistocene Asian Monsoon, Science, 274, 943–948, 1996.
Cohen, J.: A coefficient of agreement for nominal scales, Educ. Psychol. Meas., 20, 37–46, 1960.
Collins, W. D., Blackmon, M. L., Bonan, G. B., Hack, J. J., Henderson, T. B., Kiehl, J. T., Large, W. G., and McKenna, D. S.: The Community Climate System Model version 3 (CCSM3), J. Climate, 19, 2122–2143, 2006.
Conte, M. H., Sicre, M.-A., Rühlemann, C., Weber, J. C., Schulte, S., Schulz-Dull, D., and Blanz, T.: Global temperature calibration of the alkenone unsaturation index ($U^{K'}_{37}$) in surface waters and comparison with surface sediments, Geochem. Geophys. Geosy., 7, Q02005, doi:10.1029/2005GC001054, 2006.
Cortese, G., Abelmann, A., and Gersonde, R.: A glacial warm water anomaly in the subantarctic Atlantic Ocean, near the Agulhas Retroflection, Earth Planet. Sc. Lett., 222, 767–778, 2004.
Crundwell, M., Scott, G., Naish, T., and Carter, L.: Glacial-interglacial ocean climate variability from planktonic foraminifera during the Mid-Pleistocene transition in the temperate Southwest Pacific, ODP Site 1123, Palaeogeogr. Palaeocl., 260, 202–229, 2008.
De Abreu, L., Abrantes, F. F., Shackleton, N. J., Tzedakis, P. C., McManus, J. F., Oppo, D. W., and Hall, M. A.: Ocean climate variability in the eastern North Atlantic during interglacial marine isotope stage 11: A partial analogue to the Holocene?, Paleoceanography, 20, PA3009, doi:10.1029/2004PA001091, 2005.
de Villiers, S.: Dissolution effects on foraminiferal Mg/Ca records of sea surface temperature in the western equatorial Pacific, Paleoceanography, 18, 1070, 10.1029/2002PA000802 2003.
Dickson, A. J., Beer, C. J., Dempsey, C., Maslin, M. A., Bendle, J. A., McClymont, E. L., and Pancost, R. D.: Oceanic forcing of the Marine Isotope Stage 11 interglacial, Nat. Geosci., 2, 428–433, 2009.
Dudley, W. C. and Nelson, C. S.: The influence of non-equilibrium isotope fractionation on the Quaternary calcareous nannofossil stable isotope signal in the southwest Pacific Ocean, DSDP Site 594, Mar. Micropaleontol., 24, 3–27, 1994.
Dürkopp, A., Hale, W., Mulitza, S., Pätzold, J., and Wefer, G.: Late Quaternary variations of sea surface salinity and temperature in the western tropical Atlantic: evidence from δ^{18}O of Globigerinoides sacculifer, Paleoceanography, 12, 764–772, 1997.
Elderfield, H., Greaves, M., Barker, S., Hall, I. R., Tripati, A., Ferretti, P., Crowhurst, S., Booth, L., and Daunt, C.: A record of bottom water temperature and seawater δ^{18}O for the South-

CPD
9, 837–890, 2013

ern Ocean over the past 440 kyr based on Mg/Ca of benthic foraminiferal Uvigerina spp., Quaternary Sci. Rev., 29, 160–169, 2010.
Elderfield, H., Ferretti, P., Greaves, M., Crowhurst, S., McCave, I. N., Hodell, D., and Piotrowski, A. M.: Evolution of ocean temperature and ice volume through the Mid-Pleistocene climate transition, Science, 337, 704–709, 2012.
Emeis, K.-C., Doose, H., Mix, A., and Schulz-Bull, D.: Alkenone sea-surface temperatures and carbon burial at site 846 (eastern equatorial Pacific Ocean): the last 1.3 M.Y., Proc. ODP, Sci. Results, 138, 605–613, 1995.
EPICA community members: Eight glacial cycles from an Antarctic ice core, Nature, 429, 623–628, 2004.
Garidel-Thoron, T. D., Rosenthal, Y., Bassinot, F., and Beaufort, L.: Stable sea surface temperatures in the western Pacific warm pool over the past 1.75 million years, Nature, 433, 294–298, 2005.
Hale, W. and Pflaumann, U.: Sea-surface Temperature Estimations using a Modern Analog Technique with Foraminiferal Assemblages from Western Atlantic Quaternary Sediments, in: Use of Proxies in Paleoceanography – Examples from the South Atlantic, edited by: Fischer, G. and Wefer, G., Spinger, Berlin, Heidelberg, 69–90, 1999.
Hall, I. R., McCave, I. N., Shackleton, N. J., Weedon, G. P., and Harris, S. E.: Intensified deep Pacific inflow and ventilation in Pleistocene glacial times, Nature, 412, 809–812, 2001.
Hammer, O. and Harper, D. A. T.: Paleontological Data Analysis, Blackwell Publishing, Malden, Oxford, Victoria, 2006.
Hammer, O., Harper, D. A. T., and Ryan, P. D.: PAST: Palaeontological statistics package for education and data analysis, Paleaeontol. Electron., 4, 1–9, 2001.
Hannachi, A., Jolliffe, I. T., and Stephenson, D. B.: Empirical orthogonal functions and related techniques in atmospheric science: A review, Int. J. Climatol., 27, 1119–1152, 2007.
Hao, Q., Wang, L., Oldfield, F., Peng, S., Qin, L., Song, Y., Xu, B., Qiao, Y., Bloemendal, J., and Guo, Z.: Delayed build-up of Arctic ice sheets during 400,000-year minima in insolation variability, Nature, 490, 393–396, 2012.
Haug, G. H.: Zur Paläo-Ozeanographie und Sedimentationsgeschichte im Nordwest-Pazifik während der letzten 6 Millionen Jahre (ODP-Site 882), Ph.D., Mathematisch-Naturwissenschaftliche Fakultät, Christian-Albrechts-Universität, Kiel, 98 pp., 1995.
Hays, J. D., Imbrie, J., and Shackleton, N. J.: Variations in the Earth's orbit: Pacemaker of the Ice Ages, Science, 194, 1121–1132, 1976.

CPD
9, 837–890, 2013

Hayward, B. W., Scott, G. H., Crundwell, M. P., Kennett, J. P., Carter, L., Neil, H. L., Sabaa, A. T., Wilson, K., Rodger, J. S., Schaefer, G., Grenfell, H. R., and Li, Q.: The effect of submerged plateaux on Pleistocene gyral circulation and sea-surface temperatures in the Southwest Pacific, Global Planet. Change, 63, 309–316, 2008.

Healey, S. and Thunell, R.: Millenial-scale variability in western subtropical North Atlantic surface and deep water circulation during marine isotope stages 11 and 12, Paleoceanography, 19, PA1013, doi:10.1029/2003PA000925, 2004.

Helmke, J. P., Bauch, H. A., and Erlenkeuser, H.: Development of glacial and interglacial conditions in the Nordic seas between 1.5 and 0.35 Ma, Quaternary Sci. Rev., 22, 1717–1728, 2003.

Herbert, T. D., Schuffert, J. D., Andreasen, D., Heusser, L., Lyle, M., Mix, A., Ravelo, A. C., Stott, L. D., and Herguera, J. C.: Collapse of the California Current during glacial maxima linked to climate change on land, Science, 293, 71–76, 2001.

Herbert, T. D., Cleaveland Peterson, L., Lawrence, K. T., and Liu, Z.: Tropical ocean temperatures over the past 3.5 million years, Science, 328, 1530–1534, 2010.

Hodell, D. A., Charles, C. D., and Ninnemann, U. S.: Comparison of interglacial stages in the South Atlantic sector of the southern ocean for the past 450 kyr: implifications for Marine Isotope Stage (MIS) 11, Global Planet. Change, 24, 7–26, 2000.

Hodell, D. A., Charles, C. D., Curtis, J. H., Mortyn, P. G., Ninnemann, U. S., and Venz, K. A.: Data report: Oxygen isotope stratigraphy of ODP Leg 177 Sites 1088, 1089, 1090, 1093, and 1094, Proc. ODP, Sci. Results, 177, 1–26, 2003a.

Hodell, D. A., Venz, K. A., Charles, C. D., and Ninnemann, U. S.: Pleistocene vertical carbon isotope and carbonate gradients in the South Atlantic sector of the Southern Ocean, Geochem. Geophy. Geosys., 4, 1004, doi:10.1029/2002GC000367, 2003b.

Imbrie, J. and Kipp, N. G.: A new micropaleontological method for quantitative paleoclimatology: Application to a late Pleistocene Caribbean core, in: The Late Cenozoic Glacial Ages, edited by: Turekian, K. K., Yale University Press, New Haven, Conn, 71–181, 1971.

Jahn, B.: Mid to late Pleistocene variations of marine productivity in and terrigenous input to the southeast Atlantic, Universität Bremen, Berichte aus dem Fachbereich Geowissenschaften, 2002.

Jahn, B., Donner, B., Müller, P. J., Röhl, U., Schneider, R. R., and Wefer, G.: Pleistocene variations in dust input and marine productivity in the northern Benguela Current: Evidence of evolution of global glacial-interglacial cycles, Palaeogeogr. Palaeocl., 193, 515–533, 2003.

CPD
9, 837–890, 2013

Jian, Z., Wang, P., Chen, M.-P., Li, B., Zhao, Q., Bühring, C., Laj, C., Lin, H.-L., Pflaumann, U., Bian, Y., Wang, R., and Cheng, X.: Foraminiferal responses to major Pleistocene paleoceanographic changes in the southern China Sea, Paleoceanography, 15, 229–243, 2000.

Jolliffe, I. T.: Principal Component Analysis, 2nd Edn., Springer-Verlag, New York, 487 pp., 2002.

Jouzel, J., Masson-Delmotte, V., Cattani, O., Dreyfus, G., Falourd, S., Hoffmann, G., Minster, B., Nouet, J., Barnola, J. M., Chappellaz, J., Fischer, H., Gallet, J. C., Johnsen, S., Leuenberger, M., Loulergue, L., Luethi, D., Oerter, H., Parrenin, F., Raisbeck, G., Raynaud, D., Schilt, A., Schwander, J., Selmo, E., Souchez, R., Spahni, R., Stauffer, B., Steffensen, J. P., Stenni, B., Stocker, T. F., Tison, J. L., Werner, M., and Wolff, E. W.: Orbital and millennial Antarctic climate variability over the past 800,000 years, Science, 317, 793–796, 2007.

Kandiano, E. S. and Bauch, H. A.: Surface ocean temperatures in the north-east Atlantic during the last 500 000 years: evidence from foraminiferal census data, Terra Nova, 15, 265–271, 2003.

Kandiano, E. S. and Bauch, H. A.: Phase relationship and surface water mass change in the Northeast Atlantic during Marine Isotope Stage 11 (MIS 11), Quaternary Res., 68, 445–455, 2007.

Kandiano, E. S., Bauch, H. A., Fahl, K., Helmke, J. P., Röhl, U., Pérez-Folgado, M., and Cacho, I.: The meridional temperature gradient in the eastern North Atlantic during MIS 11 and its link to the ocean–atmosphere system, Palaeogeogr. Palaeocl., 333–334, 24–39, 2012.

Kleiven, H. F., Jansen, E., Curry, W. B., Hodell, D. A., and Venz, K.: Atlantic Ocean thermohaline circulation changes on orbital to suborbital timescales during the mid-Pleistocene, Paleoceanography, 18, 1008, doi:10.1029/2001PA000629, 2003.

Kunz-Pirrung, M., Gersonde, R., and Hodell, D. A.: Mid-Brunhes century-scale diatom sea surface temperature and sea ice records from the Atlantic sector of the Southern Ocean (ODP Leg 177, sites 1093, 1094 and core PS2089-2), Palaeogeogr. Palaeocl., 182, 305–328, 2002.

Laepple, T., Werner, M., and Lohmann, G.: Synchronicity of Antarctic temperatures and local solar insolation on orbital timescales, Nature, 471, 91–94, 2011.

Laskar, J., Robutel, P., Joutel, F., Gastineau, M., Correia, A. C. M., and Levrard, B.: A long term numerical solution for the insolation quantities of the Earth, Astron. Astrophys., 428, 261–285, 2004.

CPD
9, 837–890, 2013

Lawrence, K. T., Liu, Z., and Herbert, T. D.: Evolution of the eastern tropical Pacific through Plio-Pleistocene glaciation, Science, 312, 79–83, 2006.
Lawrence, K. T., Herbert, T. D., Brown, C. M., Raymo, M. E., and Haywood, A. M.: High amplitude variations in North Atlantic sea surface temperature during the early Pliocene Warm Period, Paleoceanography, 24, PA2218, doi:10.1029/2008PA001669, 2009.
Lawrence, K. T., Sosdian, S., White, H. E., and Rosenthal, Y.: North Atlantic climate evolution through the Plio-Pleistocene climate transitions, Earth Planet. Sc. Lett., 300, 329–342, 2010.
Le, J. and Shackleton, N. J.: Carbonate dissolution fluctuations in the western equatorial Pacific during the late Quaternary, Paleoceanography, 7, 21–42, 1992.
Lea, D. W., Pak, D. K., and Spero, H. J.: Climate impact of late Quaternary equatorial Pacifc sea surface temperature variations, Science, 289, 1719–1724, 2000.
Li, L., Wang, H., Li, J. R., Zhao, M., and Wang, P.: Changes in sea surface temperature in western South China Sea over the past 450 ka, Chinese Sci. Bull., 54, 3335–3343, 2009.
Li, L., Li, Q., Tian, J., Wang, P., Wang, H., and Liu, Z.: A 4-Ma record of thermal evolution in the tropical western Pacific and its implications on climate change, Earth Planet. Sc. Lett., 309, 10–20, 2011.
Lisiecki, L. E. and Raymo, M. E.: A Pliocene-Pleistocene stack of 57 globally distributed benthic δ^{18}O records, Paleoceanography, 20, PA1003, doi:10.1029/2004PA001071, 2005.
Lisiecki, L. E., Raymo, M. E., and Curry, W. B.: Atlantic overturning responses to Late Pleistocene climate forcings, Nature, 456, 85–88, 2008.
Liu, Z. and Herbert, T. D.: High-latitude influence on the eastern equatorial Pacific climate in the early Pleistocene epoch, Nature, 427, 729–723, 2004.
Lohmann, G., Pfeiffer, M., Laepple, T., Leduc, G., and Kim, J.-H.: A model-data comparison of the Holocene global sea surface temperature evolution, Clim. Past Discuss., 8, 1005–1056, doi:10.5194/cpd-8-1005-2012, 2012.
Lourergue, L., Schilt, A., Spahni, R., Masson-Delmotte, V., Blunier, T., Lemieux, B., Barnola, J.-M., Raynaud, D., Stocker, T. F., and Chappellaz, J.: Orbital and millennial-scale features of atmospheric CH_4 over the past 800,000 years, Nature, 453, 383–386, 2008.
Loutre, M. F. and Berger, A.: Marine Isotope Stage 11 as an analogue for the present interglacial, Global Planet. Change, 36, 209–217, 2003.
Maiorano, P., Tarantino, F., Marino, M., and De Lange, G. J.: Paleoenvironmental conditions at Core KC01B (Ionian Sea) through MIS 13-9: Evidence from calcareous nannofossil assemblages, Quatern. Int., doi:10.1016/j.quaint.2011.12.007, in press, 2012.

CPD
9, 837–890, 2013

Malmgren, B. A. and Nordlund, U.: Application of artificial neural networks to paleoceanographic data, Palaeogeogr. Palaeocl., 136, 359–373, doi:10.1016/s0031-0182(97)00031-x, 1997.
Malmgren, B. A., Kucera, M., Nyberg, J., and Waelbroeck, C.: Comparison of statistical and Artificial Neural Network techniques for estimating past sea surface temperatures from planktonic foraminifer census data, Paleoceanography, 16, 520–530, doi:10.1029/2000pa000562, 2001.
Martrat, B., Grimalt, J. O., Shackleton, N. J., de Abreu, L., Hutterli, M. A., and Stocker, T. F.: Four climate cycles of recurring deep and surface water destabilizations on the Iberian Margin, Science, 317, 502–507, 2007.
McIntyre, K., Ravelo, A. C., and Delaney, M. L.: North Atlantic intermediate waters in the late Pliocene to early Pleistocene, Paleoceanography, 14, 324–335, doi:10.1029/1998PA900005, 1999.
McManus, J. F., Oppo, D. W., and Cullen, J. L.: A 0.5-million-year record of millennial-scale climate variability in the North Atlantic, Science, 283, 971–975, 1999.
Medina-Elizalde, M. and Lea, D. W.: The Mid-Pleistocene transition in the tropical Pacific, Science, 310, 1009–1012, 2005.
Merkel, U., Prange, M., and Schulz, M.: ENSO variability and teleconnections during glacial climates, Quaternary Sci. Rev., 29, 86–100, 2010.
Mix, A. C., Le, J., and Shackleton, N. J.: Benthic foraminiferal stable isotope stratigraphy of Site 846: 0–1.8 Ma, Proc. ODP, Sci. Results, 138, 839–854, 1995.
Müller, P. J., Kirst, G., Ruhland, G., v. Storch, I., and Rosell-Melé, A.: Calibration of the alkenone paleotemperature index $U^{K'}_{37}$ based on core-tops from the eastern South Atlantic and the global ocean (60° N–60° S), Geochim. Cosmochim. Acta, 62, 1757–1772, 1998.
Naafs, B. D. A., Hefter, J., Ferretti, P., Stein, R., and Haug, G. H.: Sea surface temperatures did not control the first occurrence of Hudson Strait Heinrich Events during MIS 16, Paleoceanography, 26, PA4201, doi:10.1029/2011PA002135, 2011.
Niebler, H.-S.: Rekonstruktion von Paläo-Umweltparametern anhand von stabilen Isotopen und Faunenvergesellschaftungen planktischer Foraminiferen im Südatlantik, Ber. Polarforsch., 167, 1–198, 1995.
Niitsuma, N., Oba, T., and Okada, M.: Oxygen and carbon isotope stratigraphy at site 723, Oman Margin, Proc. ODP, Sci. Results, 117, 321–341, 1991.

CPD
9, 837–890, 2013

Nürnberg, D. and Groeneveld, J.: Pleistocene variability of the Subtropical Convergence at East Tasman Plateau: Evidence from planktonic foraminiferal Mg/Ca (ODP Site 1172A), Geochem. Geophy. Geosys., 7, Q04P11, doi:10.1029/2005GC000984, 2006.

Nürnberg, D., Brughmans, N., Schönfeld, J., Ninnemann, U., and Dullo, C.: Paleo-export production, terrigenous flux and sea surface temperatures around Tasmania – implications for Glacial/Interglacial changes in the Subtropical Convergence Zone, in: The Cenozoic Southern Ocean: Tectonics, Sedimentation and Climate Change between Australia and Antarctica, edited by: Exon, N., Kennett, J., and Malone, M., Geophysical Monograph Series, 151, American Geophysical Union, Washington, DC, 291–318, 2004.

O'ishi, R. and Abe-Ouchi, A.: Polar amplification in the mid-Holocene derived from dynamical vegetation change with a GCM, Geophys. Res. Lett., 38, L14702, doi:10.1029/2011GL048001, 2011.

Oleson, K. W., Niu, G.-Y., Yang, Z.-L., Lawrence, D. M., Thornton, P. E., Lawrence, P. J., Stöckli, R., Dickinson, R. E., Bonan, G. B., Levis, S., Dai, A., and Qian, T.: Improvements to the Community Land Model and their impact on the hydrological cycle, J. Geophys. Res., 113, G01021, doi:10.1029/2007JG000563, 2008.

Oppo, D. W., McManus, J. F., and Cullen, J. L.: Abrupt climate events 500,000 to 340,000 years ago: Evidence from subpolar North Atlantic sediments, Science, 279, 1335–1338, 1998.

Oppo, D. W., Linsley, B. K., Rosenthal, Y., Dannenmann, S., and Beaufort, L.: Orbital and suborbital climate variability in the Sulu Sea, western tropical Pacific, Geochem. Geophy. Geosy., 4, 1003, doi:10.1029/2001GC000260, 2003.

Otto-Bliesner, B. L., Tomas, R., Brady, E. C., Ammann, C., Kothavala, Z., and Clauzet, G.: Climate sensitivity of moderate- and low-resolution versions of CCSM3 to preindustrial forcings, J. Climate, 19, 2567–2583, 2006.

Paillard, D., Labeyrie, L., and Yiou, P.: Macintosh program performs time-series analysis, EOS Trans. Am. Geophys. Union, 77, 379, 1996.

Parrenin, F., Barnola, J.-M., Beer, J., Blunier, T., Castellano, E., Chappellaz, J., Dreyfus, G., Fischer, H., Fujita, S., Jouzel, J., Kawamura, K., Lemieux-Dudon, B., Loulergue, L., Masson-Delmotte, V., Narcisi, B., Petit, J.-R., Raisbeck, G., Raynaud, D., Ruth, U., Schwander, J., Severi, M., Spahni, R., Steffensen, J. P., Svensson, A., Udisti, R., Waelbroeck, C., and Wolff, E.: The EDC3 chronology for the EPICA Dome C ice core, Clim. Past, 3, 485–497, doi:10.5194/cp-3-485-2007, 2007.

CPD
9, 837–890, 2013

Pelejero, C., Calvo, E., Barrows, T. T., Logan, G. A., and De Deckker, P.: South Tasman Sea alkenone palaeothermometry over the last four glacial/interglacial cycles, Mar. Geol., 230, 73–86, 2006.

Petit, J. R., Jouzel, J., Raynaud, D., Barkov, N. I., Barnola, J.-M., Basile, I., Bender, M., Chappellaz, J., Davis, M., Delaygue, G., Delmotte, M., Kotlyakov, V. M., Legrand, M., Lipenkov, V. Y., Lorius, C., Pepin, L., Ritz, C., Saltzman, E., and Stievenard, M.: Climate and atmospheric history of the past 420,000 years from the Vostok ice core, Antarctica, Nature, 399, 429–435, 1999.

Pflaumann, U.: Sea-surface temperatures during the last 750,000 years in the eastern equatorial Atlantic: Planktonic foraminiferal record of Meteor – cores 13519, 13521, and 16415, in: Meteor Forschungsergebnisse, Deutsche Forschungsgemeinschaft, Reihe C Geologie und Geophysik, Gebrüder Bornträger, Berlin, Stuttgart, 137–161, 1986.

Pflaumann, U., Duprat, J., Pujol, C., and Labeyrie, L.: SIMMAX: A modern analog technique to deduce Atlantic sea surface temperatures from planktonic foraminifera in deep-sea sediments, Paleoceanography, 11, 15–35, 1996.

Pisias, N. G. and Mix, A. C.: Spatial and temporal oceanographic variability of the eastern equatorial Pacific during the late Pleistocene: evidende from Radiolaria microfossils, Paleoceanography, 12, 381–393, 1997.

Pisias, N. G. and Rea, D. K.: Late Pleistocene paleoclimatology of the central equatorial Pacific: Sea surface response to the southeast trade winds, Paleoceanography, 3, 21–37, 1988.

Pisias, N. G., Mix, A. C., and Zahn, R.: Nonlinear response in the global climate system: evidence from benthic oxygen isotopic record in core RC13-110, Paleoceanography, 5, 147–160, 1990.

Pol, K., Debret, M., Masson-Delmotte, V., Capron, E., Cattani, O., Dreyfus, G., Falourd, S., Johnsen, S., Jouzel, J., Landais, A., Minster, B., and Stenni, B.: Links between MIS 11 millennial to sub-millennial climate variability and long term trends as revealed by new high resolution EPICA Dome C deuterium data – A comparison with the Holocene, Clim. Past, 7, 437–450, doi:10.5194/cp-7-437-2011, 2011.

Prell, W. L.: The stability of low-latitude sea-surface temperatures: An evaluation of the CLIMAP reconstruction with emphasis on the positive SST anomalies, Department of Energy, Washington, DC, 1985.

Raymo, M. E. and Mitrovica, J. X.: Collapse of polar ice sheets during the stage 11 interglacial, Nature, 483, 453–456, 2012.

CPD
9, 837–890, 2013

Raymo, M. E., Ganley, K., Carter, S., Oppo, D. W., and McManus, J.: Millennial-scale climate instability during the early Pleistocene epoch, Nature, 392, 699–702, 1998.

Raymo, M. E., Oppo, D. W., Flower, B. P., Hodell, D. A., McManus, F. J., Venz, K. A., Kleiven, H. F., and McIntyre, K.: Stability of North Atlantic water masses in face of pronounced climate variability during the Pleistocene, Paleoceanography, 19, PA2008, doi:10.1029/2003PA000921, 2004.

Rincón-Martínez, D., Lamy, F., Contreras, S., Leduc, G., Bard, E., Saukel, C., Blanz, T., Mackensen, A., and Tiedemann, R.: More humid interglacials in Ecuador during the past 500 kyr linked to latitudinal shifts of the equatorial front and the Intertropical Convergence Zone in the eastern tropical Pacific, Paleoceanography, 25, PA2210, doi:10.1029/2009PA001868, 2010.

Rodrigues, T., Voelker, A. H. L., Grimalt, J. O., Abrantes, F., and Naughton, F.: Iberian Margin sea surface temperature during MIS 15 to 9 (580–300 ka): Glacial suborbital variability versus interglacial stability, Paleoceanography, 26, PA1204, doi:10.1029/2010PA001927, 2011.

Rohling, E. J., Grant, K., Bolshaw, M., Roberts, A. P., Siddall, M., Hemleben, C., and Kucera, M.: Antarctic temperature and global sea level closely coupled over the past five glacial cycles, Nat. Geosci., 2, 500–504, doi:10.1038/ngeo557, 2009.

Rohling, E. J., Braun, K., Grant, K., Kucera, M., Roberts, A. P., Siddall, M., and Trommer, G.: Comparison between Holocene and Marine Isotope Stage-11 sea-level histories, Earth Planet. Sc. Lett., 291, 97–105, 2010.

Ruddiman, W. F., Shackleton, N. J., and McIntyre, A.: North Atlantic sea-surface temperatures for the last 1.1 million years, in: North Atlantic Palaeoceanography, edited by: Summerhayer, C. P. and Shackleton, N. J., Geological Society Special Publication, 155–173, 1986.

Ruddiman, W. F., Raymo, M. E., Martinson, G. D., Clement, B. M., and Backman, J.: Pleistocene evolution: Northern Hemisphere ice sheets and North Atlantic Ocean, Paleoceanography, 4, 353–412, 1989.

Russon, T., Elliot, M., Sadekov, A., Cabioch, G., Corrège, T., and De Deckker, P.: Inter-hemispheric asymmetry in the early Pleistocene Pacific warm pool, Geophys. Res. Lett., 37, L11601, doi:10.1029/2010GL043191, 2010.

Sarnthein, M., Erlenkeuser, H., von Grafenstein, R., and Schröder, C.: Stable isotope stratigraphy for the last 750.000 years, Meteor core 13519 from the eastern equatorial Atlantic., Meteor Forschungsergebnisse, Deutsche Forschungsgemeinschaft, Reihe C Geologie und Geophysik, Gebrüder Bornträger, Berlin, Stuttgart, 1984.

CPD
9, 837–890, 2013

Schaefer, G., Rodger, J. S., Hayward, B. W., Kennett, J. P., Sabaa, A. T., and Scott, G. H.: Planktic foraminiferal and sea surface temperature record during the last 1 Myr across the Subtropical Front, Southwest Pacific, Mar. Micropaleontol., 54, 191–212, 2005.
Schilt, A., Baumgartner, M., Blunier, T., Schwander, J., Spahni, R., Fischer, H., and Stocker, T. F.: Glacial–interglacial and millennial-scale variations in the atmospheric nitrous oxide concentration during the last 800,000 years, Quaternary Sci. Rev., 182–192, 2010.
Schmidt, M. W., Vautravers, M. J., and Spero, H. J.: Western Caribbean sea surface temperatures during the late Quaternary, Geochem. Geophy. Geosys., 7, Q02P10, doi:10.1029/2005GC000957, 2006.
Sepulcre, S., Tachikawa, K., Vidal, L., Thouveny, N., and Bard, E.: Preservation state of metastable magnesian calcite in periplatform sediments from the Caribbean Sea over the last million years, Geochem. Geophy. Geosys., 10, Q11013, doi:10.1029/2009GC002779, 2009.
Sepulcre, S., Vidal, L., Tachikawa, K., Rostek, F., and Bard, E.: Sea-surface salinity variations in the northern Caribbean Sea across the Mid-Pleistocene Transition, Clim. Past, 7, 75–90, doi:10.5194/cp-7-75-2011, 2011.
Shackleton, N. J. and Hall, M. A.: Oxygen and carbon isotope stratigraphy of Deep Sea Drilling Project Hole 552A: Plio-Pleistocene glacial history, Initial Rep., Deep Sea Res., 81, 599–609, 1984.
Shiau, L.-J., Yu, P.-S., Wei, K.-Y., Yamamoto, M., Lee, T.-Q., Yu, E.-F., Fang, T.-H., and Chen, M.-T.: Sea surface temperature, productivity, and terrestrial flux variations of the southeastern South China Sea over the past 800,000 years (IMAGESMD972142), Terr. Atmos. Ocean. Sci., 19, 363–376, 2008.
Siegenthaler, U., Stocker, T. F., Monnin, E., Lüthi, D., Schwander, J., Stauffer, B., Raynaud, D., Bamola, J.-M., Fischer, H., Masson-Delmotte, V., and Jouzel, J.: Stable carbon cycle – climate relationship during the Late Pleistocene, Science, 310, 1313–1317, 2005.
Stein, R., Hefter, J., Grützner, J., Voelker, A., and Naafs, B. D. A.: Variability of surface water characteristics and Heinrich-like events in the Pleistocene midlatitude North Atlantic Ocean: Biomarker and XRD records from IODP Site U1313 (MIS 16-9), Paleoceanography, 24, PA2203, doi:10.1029/2008PA001639, 2009.
Spooner, M. I., De Deckker, P., Barrows, T. T., and Fifield, L. K.: The behaviour of the Leeuwin Current offshore NW Australia during the last five glacial-interglacial cycles, Global Planet. Change, 75, 119–132, 2011.

CPD
9, 837–890, 2013

Sundqvist, H. S., Zhang, Q., Moberg, A., Holmgren, K., Körnich, H., Nilsson, J., and Brattström, G.: Climate change between the mid and late Holocene in northern high latitudes – Part 1: Survey of temperature and precipitation proxy data, Clim. Past, 6, 591–608, doi:10.5194/cp-6-591-2010, 2010.

Tian, J., Wang, P., Cheng, X., and Li, Q.: Astronomically tuned Plio-Pleistocene benthic δ^{18}O record from South China Sea and Atlantic-Pacific comparison, Earth Planet. Sc. Lett., 203, 1015–1029, 2002.

Tzedakis, P. C.: The MIS 11–MIS 1 analogy, southern European vegetation, atmospheric methane and the "early anthropogenic hypothesis", Clim. Past, 6, 131–144, doi:10.5194/cp-6-131-2010, 2010.

Tzedakis, P. C., Raynaud, D., McManus, J. F., Berger, A., Brovkin, V., and Kiefer, T.: Interglacial diversity, Nat. Geosci., 2, 751–755, 2009.

Vázquez Riveiros, N., Waelbroeck, C., Skinner, L., Roche, D. M., Duplessy, J.-C., and Michel, E.: Response of South Atlantic deep waters to deglacial warming during Terminations V and I, Earth Planet. Sc. Lett., 298, 323–333, 2010.

Venz, K. A., Hodell, D. A., Stanton, C., and Warnke, D. A.: A 1.0 Myr record of glacial North Atlantic intermediate water variability from ODP site 982 in the northeast Atlantic, Paleoceanography, 14, 42–52, 1999.

Voelker, A. and De Abreu, L.: A review of abrupt climate change events in the Northeastern Atlantic Ocean (Iberian Margin): latitudinal, longitudinal and vertical gradients, in: Understanding the Causes, mechanisms and extent of the Abrupt Climate Change, edited by: Rashid, H., Polyak, L., and Mosley-Thompson, E., AGU Geophysical Monograph, Washington DC, 15–38, 2011.

Voelker, A., Martin, P., Lebreiro, S., and Abrantes, F.: Millennial scale deep/intermediate water changes at the mid-depth Portuguese margin during Marine Isotope Stage (MIS) 11, Quatern. Int., 436, 167–168, 2007.

Voelker, A. H. L., Rodrigues, T., Billups, K., Oppo, D., McManus, J., Stein, R., Hefter, J., and Grimalt, J. O.: Variations in mid-latitude North Atlantic surface water properties during the mid-Brunhes (MIS 9-14) and their implications for the thermohaline circulation, Clim. Past, 6, 531–552, doi:10.5194/cp-6-531-2010, 2010.

von Grafenstein, R., Zahn, R., Tiedemann, R., and Murat, A.: Planktonic δ^{18}O records at sites 976 and 977, Alboran Sea: Stratigraphy, forcing, and paleoceanographic implications, Proc. ODP, Sci. Results, 161, 469–479, 1999.

CPD
9, 837–890, 2013

Waelbroeck, C., Labeyrie, L., Duplessy, J.-C., Guiot, J., Labracherie, M., Leclaire, H., and Duprat, J.: Improving past sea surface temperature estimates based on planktonic fossil faunas, Paleoceanography, 13, 272–283, 1998.

Weller, P.: Variability of paleoproductivity, paleotemperature and terrestrial organic matter supply in the mid-Pleistocene southern south Atlantic: Implications from biomarker records (ODP-LEG 177), Ph.D., Alfred-Wegener-Institut für Polar- und Meeresforschung, Universität Bremen, Bremerhaven, 169 pp., 2006.

Yeager, S. G., Shields, C. A., Large, W. G., and Hack, J. J.: The low-resolution CCSM3, J. Climate, 19, 2545–2466, 2006.

Zhang, Q., Sundqvist, H. S., Moberg, A., Körnich, H., Nilsson, J., and Holmgren, K.: Climate change between the mid and late Holocene in northern high latitudes – Part 2: Model-data comparisons, Clim. Past, 6, 609–626, doi:10.5194/cp-6-609-2010, 2010.

CPD
9, 837–890, 2013

Table 1. Summary of the MIS11 SST records used in this study. Longitude, latitude, and water depth of each record are provided. The type of $\delta^{18}O$ records used for the age model tuning, the quality of the age models (expressed as the correlation coefficients of the stable isotope records with the LR04 stack; Lisiecki and Raymo, 2005), and the temporal resolution of the age models and SST data is indicated. Records used for the Empirical Orthogonal Function (EOF) analysis are marked with an asterisk, those used for the proxy–data model comparison with an x; also given are the total number of available data points and types of SST records used in the study.

Record	Longitude	Latitude	Water depth	$\delta^{18}O$ record used for age model tuning	Reference ($\delta^{18}O$ record)	Quality/resolution of records				Data used for proxy-model comparison [x] and EOF[*]				Type of SST record	Reference (SST record)
						age model quality – 200–500 ka	age model quality – investigated time interval	age model resolution (kyr)	SST data resolution (kyr)	annual SST data	summer SST data	winter SST data	total no. of proxy data used for proxy-model comparison		
DSDP 90-594	174.95	−45.52	1204	*Uvigerina* spp.	Dudley and Nelson (1994)	0.85	0.89	4.30	2.1	x*	x SH		21	MAT	Schaefer et al. (2005); Hayward et al. (2008)
DSDP 91-607	−32.96	41.00	3427	*C. wuellerstorfi*, *C. kullenbergi*	Ruddiman et al. (1989)	0.93	0.97	3.10	2.5 ($U^{K'}_{37}$); 2.8 (TF)	x*	x	x	8 (TF); 11 ($U^{K'}_{37}$)	$U^{K'}_{37}$; TF – foraminiferal assemblages	Lawrence et al. (2010); Ruddiman et al. (1989)
E49-18	90.15	−46.05	1459	*G. bulloides*	Hays et al. (1976)	0.92	0.95	3.00	3.2		x* SH		7	TF – radiolarian assemblages	Hays et al. (1976)
FR194-GC3	149.98	−44.25	2667	*G. bulloides*	Pelejero et al. (2006)	0.78	0.91	4.60	4.6	x*			5	$U^{K'}_{37}$	Pelejero et al. (2006)
GeoB1312	−29.66	−31.66	3436	*C. wuellerstorfi*	Hale and Pflaumann (1999)	0.96	0.97	3.90	3.9		x* SH	x SH	8	MAT[h]	Hale and Pflaumann (1999)
GeoB1722	11.75	−29.45	3973	*C. wuellerstorfi*	Bickert and Mackensen (2003)	0.96	0.96	1.40	1.8	x*			23	$U^{K'}_{37}$	Jahn (2002)
GeoB2204	−34.02	−8.53	2072	*G. sacculifer*	Dürkopp et al. (1997)	0.92	0.94	3.50	6.6		x	x	5	MAT[h]	Hale and Pflaumann (1999)
GIK13519	−19.85	5.67	2860	*G. sacculifer*	Sarnthein et al. (1984)	0.88	0.87	8.60	5.6		x* SH	x SH	6	TF – foraminiferal assemblages	Pflaumann (1986)
GIK17957	115.31	10.90	2195	*G. sacculifer*	Jian et al. (2000)	0.62	0.87	10.90	5.6		x*	x	10	TF – foraminiferal assemblages[i]	Jian et al. (2000)
GIK23414	−20.29	53.54	2199	*C. wuellerstorfi*	Kandiano and Bauch (2007)	0.94	0.94	0.40	0.4		x	x	68	MAT, TFT, RAM[f]	Kandiano and Bauch (2007)
IODP U1313	−32.96	41.00	3426	*C. wuellerstorfi*	Voelker et al. (2010)	0.92	0.88	0.34	0.4	x*			106	$U^{K'}_{37}$	Naafs et al. (2011)
K708-7	−24.08	53.93	3502	*N. pachyderma*	Ruddiman et al. (1986)	0.86	0.71	4.90	4		x*	x	9	TF – foraminiferal assemblages	Ruddiman et al. (1986)
MD00-2361	113.48	−22.08	1805	*G. ruber*	Spooner et al. (2011)	0.80	0.91	3.47	5.5	x*	x SH	x SH	10	MAT	Spooner et al. (2011)
MD01-2443	−10.18	37.88	2952	Benthic[c]/ *G. bulloides*	De Abreu et al. (2005); Voelker and De Abreu (2011)	0.96/ 0.83	0.97/ 0.85	0.47/ 0.32	0.43/0.37 (TF); 0.35 ($U^{K'}_{37}$)	x	x	x	110/136 (TF)/131 ($U^{K'}_{37}$)	MAT[h]; $U^{K'}_{37}$	De Abreu et al. (2005); Voelker and De Abreu (2011); Martrat et al. (2007)
MD03-2628	−77.71	17.36	846	*G. ruber*	Sepulcre et al. (2009)	0.90	0.98	6.70	6.7	x*			7	$U^{K'15}_{37}$	Sepulcre et al. (2011)
MD03-2699	−10.66	39.04	1865	*C. wuellerstorfi*, *C. pachyderma*[b,g]	Voelker et al. (2010)	0.46[g]	0.72[g]	0.35	0.4	x*			109	$U^{K'}_{37}$	Voelker et al. (2010); Rodrigues et al. (2011)
MD05-2901	110.74	14.38	1454	*G. ruber*	Li et al. (2009)	0.79	0.79	1.20	1.3	x*			22	$U^{K'}_{37}$	Li et al. (2009)
MD06-3018	166.15	−23.00	2470	*C. wuellerstorfi*[a]	Russon et al. (2010)	0.97	0.97	4.60	4.6	x*			8	Mg/Ca of *G. ruber*	Russon et al. (2010)
MD07-3077	−14.22	−44.15	3770	*G. bulloides*, *N. pachyderma*	Vázquez Riveiros et al. (2010)	0.93	0.90	0.40	1.2		x SH		23	Percentages of *N. pachyderma*	Vázquez Riveiros et al. (2010)
MD96-2048	34.02	−26.17	660	*C. wuellerstorfi*	Caley et al. (2011)	0.73	0.85	5.00	3.8	*				stack of $U^{K'}_{37}$, Mg/Ca and Tex^{H}_{86}	Caley et al. (2011)
MD96-2077	31.25	−33.17	3781	*G. inflata*	Bard and Rickaby (2009)	0.79	0.89	2.60	2.9	x*			11	$U^{K'}_{37}$	Bard and Rickaby (2009)
MD96-2085[d]	12.94	−29.70	3001	*G. inflata*	Chen et al. (2002)	0.91	0.91	1.80	2.3		x SH		21	TF – foraminiferal assemblages	Chen et al. (2002)
MD97-2140	141.77	2.03	2547	*G. ruber*	Garidel-Thoron et al. (2005)	0.97	0.98	5.10	5.4	x*			5	Mg/Ca of *G. ruber*	Garidel-Thoron et al. (2005)
MD97-2142	119.47	12.69	1557	*G. ruber*	Shiau et al. (2008)[f]; Chen et al. (2003)	0.84/ 0.80	0.86/ 0.86	1.7/ 1.3	2.5 ($U^{K'}_{37}$)/ 2.2 (TF)	x*	x	x	19 ($U^{K'}_{37}$; 19 TF)	$U^{K'}_{37}$; TF – foraminiferal assemblages	Shiau et al. (2008)[f]; Chen et al. (2003)
MD99-2277	−6.32	69.25		*G. umbonata*	Kandiano et al. (2012)	0.76	0.93	0.83	1.73 ($U^{K'}_{37}$); 1.12 (TF)	x		x; 31 (TF)	22 ($U^{K'}_{37}$);	$U^{K'}_{37}$; TF – foraminiferal assemblages	Kandiano et al. (2012)
ODP 722	59.80	16.62	2033	*G. sacculifer*	Clemens et al. (1996)	0.92	0.97	4.80	1.5	x*			13	$U^{K'}_{37}$	Herbert et al. (2010)
ODP 723	57.61	18.05	816	*P. obliquiloculata*	Niitsuma et al. (1991)	0.92	0.82	2.10	9.2	*			4	$U^{K'}_{37}$	Emeis et al. (1995)
ODP 806	159.36	0.32	2520	*G. ruber*	Lea et al. (2000); Medina-Elizalde and Lea (2005)	0.90	0.93	5.30	3	x*			12	Mg/Ca of *G. ruber*	Lea et al. (2000); Medina-Elizalde and Lea (2005)
ODP 846	−90.82	−3.10	3296	*C. wuellerstorfi*	Mix et al. (1995)	0.92	0.96	2.40	2.4	x*			17	$U^{K'}_{37}$	Liu and Herbert (2004); Lawrence et al. (2006); Herbert et al. (2010)
ODP 882	167.60	50.36	3255	*Uvigerina* spp.	Haug (1995)	0.50	0.94	15.90	6.6	x*			4	$U^{K'}_{37}$	Haug (1995)
ODP 958	−20.00	24.00	3795	*C. wuellerstorfi*	Kandiano et al. (2012)	0.97	0.97	1.24	1.7 ($U^{K'}_{37}$); 1.5 (TF)	x*		x	28 ($U^{K'}_{37}$); 28 (TF)	$U^{K'}_{37}$; MAT & RAM[f]	Kandiano et al. (2012)
ODP 975	4.51	38.90	2415	*G. bulloides*	Kandiano et al. (2012)	0.89	0.89	1.20	6.13 ($U^{K'}_{37}$); 1.03 (TF)	x		x	59 (TF); 8 ($U^{K'}_{37}$)	MAT & RAM[f]; $U^{K'}_{37}$	Kandiano et al. (2012)
ODP 976	−4.31	36.21	1110	*G. bulloides*	von Grafenstein et al. (1999)	0.78	0.86	4.20	4.6		*			MAT	Gonzales-Donoso, unpublished data
ODP 980	−14.70	55.48	2179	*C. wuellerstorfi*	Oppo et al. (1998); McManus et al. (1999)	0.98	0.96	0.40	0.3		x*		156	scaling of oxygen isotope record of *N. pachyderma*[e]	McManus et al. (1999)
ODP 982	−15.85	57.51	1134	*C. wuellerstorfi*, *C. kullenbergi*	Venz et al. (1999)	0.72	0.95	2.20	3.2	x*			18	$U^{K'}_{37}$	Lawrence et al. (2009)
ODP 999	−78.74	12.74	2828	*G. ruber*	Schmidt et al. (2006)	0.92	0.88	1.60	1.8	x*			20	Mg/Ca of *G. ruber*	Schmidt et al. (2006)

CPD
9, 837–890, 2013

Table 1. Continued.

Record	Longitude	Latitude	Water depth	δ^{18}O record used for age model tuning	Reference (δ^{18}O record)	Quality/resolution of records				Data used for proxy-model comparison [x] and EOF[*]				Type of SST record	Reference (SST record)
						age model quality – 200–500 ka	age model quality – investigated time interval	age model resolution (kyr)	SST data resolution (kyr)	annual SST data	summer SST data	winter SST data	total no. of proxy data used for proxy-model comparison		
ODP 1012	−118.28	32.28	1773	Benthic	Herbert et al. (2001)	0.95	0.93	1.60	1.5	x*			25	$U^{K'}_{37}$	Herbert et al. (2001)
ODP 1020	−126.43	41.00	3038	Benthic	Herbert et al. (2001)	0.98	0.97	2.50	2.5	x*			10	$U^{K'}_{37}$	Herbert et al. (2001)
ODP 1082	11.82	−21.09	1281	*G. inflata*	Jahn et al. (2003)	0.70	0.83	1.70	1.8	*			6	$U^{K'}_{37}$	Jahn (2002)
ODP 1085	13.99	−29.37	1713	*C. wuellerstorfi*	Dickson et al. (2009)	0.72	0.70	0.63	0.9	x*			40	$U^{K'}_{37}$	Dickson et al. (2009)
ODP 1089	9.89	−40.94	4620	*Cibicidoides* spp.	Hodell et al. (2003b)	0.98	0.98	0.30	2.6 ($U^{K'}_{37}$); 2.5 (TF)	x*			11	$U^{K'}_{37}$	Weller (2006); Cortese et al. (2004)
ODP 1090	8.90	−42.91	3702	*Cibicidoides* spp.	Becquey and Gersonde (2002)	0.93	0.98	2.60	2.4		x SH		14	MAT	Becquey and Gersonde (2002)
ODP 1093	5.87	−49.98	3631	*N. pachyderma*	Hodell et al. (2003a)	0.91	0.91	0.80	0.4		x* SH		80	TF – diatoms	Kunz-Pirrung et al. (2002)
ODP 1094	5.13	−53.18	2807	*N. pachyderma*	Hodell et al. (2003a)	0.77	0.61	0.48	0.5		x* SH		121	TF – diatoms	Kunz-Pirrung et al. (2002)
ODP 1123	−171.50	−41.79	3290	*U. peregrina*	Hall et al. (2001); Elderfield et al. (2010)	0.97	0.97	1.90	2.4	x*			11	ANN	Crundwell et al. (2008)
ODP 1143	113.29	9.36	2772	*C. wuellerstorfi*	Tian et al. (2002)	0.91	0.97	2.70	1.9	x*			12	$U^{K'}_{37}$	Li et al. (2011)
ODP 1146	116.27	19.46	2091	*U. peregrina*	Clemens and Prell (2003)	0.97	0.97	1.67	1.38	x*			14	$U^{K'}_{37}$	Herbert et al. (2010)
ODP 1168	144.41	−42.61	2463	*C. wuellerstorfi*	Nürnberg et al. (2004)	0.36	0.19	3.40	3.4	x*			12	Mg/Ca of *G. bulloides*	Nürnberg et al. (2004)
ODP 1172	149.93	−43.96	2622	*G. bulloides*	Nürnberg and Groeneveld (2006)	0.75	0.60	2.20	2.2	x*			10	Mg/Ca of *G. bulloides*	Nürnberg and Groeneveld (2006)
ODP 1239[d]	−82.08	−0.67	1414	*C. wuellerstorfi*	Rincón-Martínez et al. (2010)	0.96	0.90	4.10	3.6	x*			7	$U^{K'}_{37}$	Rincón-Martínez et al. (2010)
PS2076	13.47	−41.15	2109	*G. bulloides*	Niebler (1995)	0.76	0.91	12.80	12.8		*SH			TF – foraminiferal assemblages	Niebler (1995)
PS2489	8.97	−42.87	3794	*C. wuellerstorfi*, *Cibicidoides* spp., *U. peregrina*	Becquey and Gersonde (2003)	0.97	0.97	1.50	1.5		x* SH		23	MAT	Becqey and Gersonde (2003)
RC11-210	−140.10	1.82	4420	*G. tumida*	Pisias and Rea (1988)	0.86	0.92	4.10	4.8		x*	x	6	TF – radiolarian assemblages	Pisias and Rea (1988)
RC13-110	−95.65	−0.10	3231	*Cibicides* sp.	Pisias et al. (1990)	0.93	0.94	4.30	5	x*			6	TF – radiolarian assemblages	Pisias and Mix (1997)
RC17-177[d]	159.45	1.76	2600	*G. sacculifer*	Le and Shackleton (1992)	0.90	0.96	3.50	4.5	x			7	Mg/Ca of *G. ruber* and *G. sacculifer*[k]	De Villiers (2003)
V12-122	−74.40	17.00	2800	*G. sacculifer*	McIntyre and Ruddiman (1997)	0.91	0.93	6.10	5.3		x*	x	6	TF – foraminiferal assemblages	Imbrie (1997)
V22-174	−12.82	−10.07	2630	*G. sacculifer*	McIntyre and Imbrie (1997)	0.86	0.93	7.60		8	x* SH	x SH	3	TF – foraminiferal assemblages	Imbrie et al. (1997)

[a] The authors made a correction of +0.640/00 for *C. wuellerstorfi*.
[b] Isotope data of *C. pachyderma* and *C. wuellerstorfi* were grouped together in this study.
[c] De Abreu et al. (2005) measured multiple benthic species (*C. robertsonianus, U. peregrina, G. affinis, C. wuellerstorfi, C. kullenbergi, H. elegans, O. umbonatus* and *C. carinata*) and calibtrated they to *Uvigerina peregrina*.
[d] Data were taken from the original publications.
[e] The authors applied two different calibrations of their alkenone data. In this study the calibration based on Conte et al. (2006) was used.
[f] The mean of SSTs estimated with MAT and RAM data was used in this study.
[g] The original age model was used in this study.
[h] For the summer and winter SSTs the mean of two MAT estimates was used in this study.
[i] The mean of SSTs calculated with MAT, RAM and TFT was used in this study.
[j] The mean of two SSTs calibrated with different equations was used in this study.
[k] The mean of SSTs based on Mg/Ca ratios of *G. ruber* and *G. sacculifer* was used in this study.

CPD
9, 837–890, 2013

Table 2. Greenhouse gas concentrations used in forcing the CCSM3 experiments (Siegenthaler et al., 2005; Schilt et al., 2010; Lourergue et al., 2008). See also Fig. 8a.

Experiments	CO_2 (ppmv)	CH_4 (ppbv)	N_2O (ppbv)
0 ka BP	280	760	270
394 ka BP	275	550	275
405 ka BP	280	660	285
416 ka BP	275	620	270

CPD
9, 837–890, 2013

Table 3. Variances explained by the first three empirical orthogonal functions (EOF) of the MIS11 SST records, including 5 and 95 % confidence limits (see also Fig. 4). Re-calculations were made with varying age and temperature uncertainties and a random exclusion of records (jackknifing, jack5 means that five records were excluded per replication). Control run refers to analysis of raw data without consideration of uncertainties. EOF results presented in Fig. 8 and discussed in Sect. 4.1 are given in bold.

Parameter	EOF1	5 %	95 %	EOF2	5 %	95 %	EOF3	5 %	95 %
control run	*51.43*			*19.87*			*6.91*		
1000, 3 kyr, 1 °C	48.72	46.86	50.60	18.77	17.32	20.39	7.49	6.54	8.57
1000, 3 kyr, 2 °C	44.49	42.04	46.98	17.59	15.46	19.72	7.91	6.66	9.30
1000, 5 kyr, 1 °C	**48.49**	**46.54**	**50.59**	**18.90**	**17.19**	**20.68**	**7.45**	**6.42**	**8.56**
1000, 5 kyr, 2 °C	44.14	41.57	46.73	17.83	15.63	20.00	7.90	6.71	9.32
1000, 5 kyr, 4 °C	35.46	32.07	38.78	15.91	13.35	18.54	8.64	7.08	10.53
1000, 6 kyr, 1 °C	48.42	46.33	50.66	18.94	17.03	20.89	7.46	6.41	8.62
1000, 6 kyr, 2 °C	44.01	41.31	46.60	17.83	15.45	20.15	7.91	6.59	9.42
1000, 5 kyr, 1 °C, jack5	48.56	45.75	51.66	18.94	16.46	21.35	7.55	6.36	8.81
1000, 5 kyr, 1 °C, jack15	49.00	44.01	53.75	18.97	15.38	22.63	7.85	6.21	9.63
1000, 5 kyr, 1 °C, jack25	49.63	42.76	55.79	19.39	14.14	24.91	8.21	6.13	10.68
1000, 5 kyr, 1 °C, jack35	51.30	41.66	61.43	20.18	13.28	27.59	9.14	6.50	12.64

CPD
9, 837–890, 2013

Table 4. Correlation coefficients and Cohen's values between the proxy and model SST anomalies for the three MIS11 time slices (Table 2), as well as a comparison of variances in the proxy and model data (statistically significant values are given in bold).

	Correlation			Cohen's Kappa			Variance			
Temperature anomaly	r/ρ	p-value	Correlation method	κ	Agreement quality (Altman, 1991)	p-value	Variance proxy data	Variance model data	F-value	p-value
390–400 ka annual	0.210	0.2254	Pearson	−0.145	poor	0.2650	**0.65**	**0.07**	**90.47**	**< 0.0001**
390–400 ka summer	**0.555**	**0.0257**	**Spearman**	0.333	fair	0.1460	**0.86**	**0.17**	**52.47**	**0.0028**
390–400 ka winter	0.301	0.1624	Pearson	−0.017	poor	0.9320	**2.02**	**0.09**	**23.65**	**< 0.0001**
400–410 ka annual	−0.157	0.3667	Spearman	−0.138	poor	0.2950	**0.60**	**0.02**	**36.26**	**< 0.0001**
400–410 ka summer	−0.006	0.9827	Spearman	−0.231	poor	0.2420	**2.72**	**0.03**	**107.59**	**< 0.0001**
400–410 ka winter	**0.425**	**0.0433**	**Spearman**	0.214	fair	0.1900	**2.07**	**0.03**	**73.62**	**< 0.0001**
410–420 ka annual	−0.039	0.8260	Spearman	−0.201	poor	0.1600	**1.17**	**0.05**	**23.90**	**< 0.0001**
410–420 ka summer	**0.636**	**0.0081**	**Spearman**	0.394	fair	0.0910	**0.40**	**0.11**	**3.71**	**0.0156**
410–420 ka winter	0.387	0.0800	Spearman	0.261	fair	0.1150	**1.93**	**0.07**	**26.06**	**< 0.0001**

CPD
9, 837–890, 2013

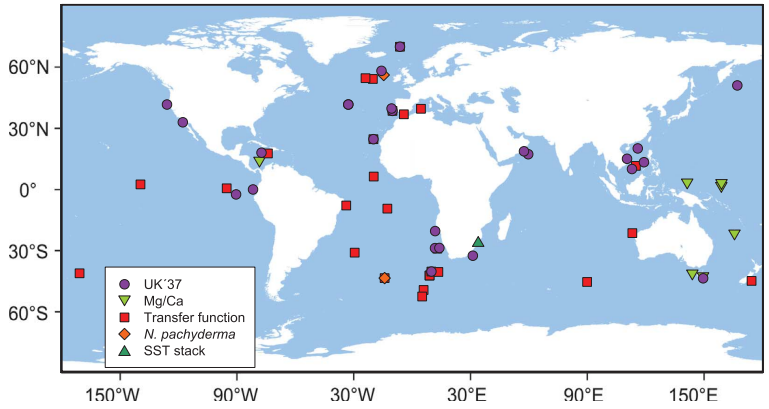

Fig. 1. Position of the sea surface temperature (SST) records used in this study. The compilation contains SST records based on Mg/Ca, $U^{k'}_{37}$, transfer functions (TF) including Artificial Neural Network (ANN), scaling of oxygen isotopes values in *Neogloboquadrina pachyderma* and percentages of *N. pachyderma* (see Sect. 2.1), and one SST stack based the mean of Mg/Ca, $U^{k'}_{37}$ and TEX^{H}_{86} (Table 1).

CPD
9, 837–890, 2013

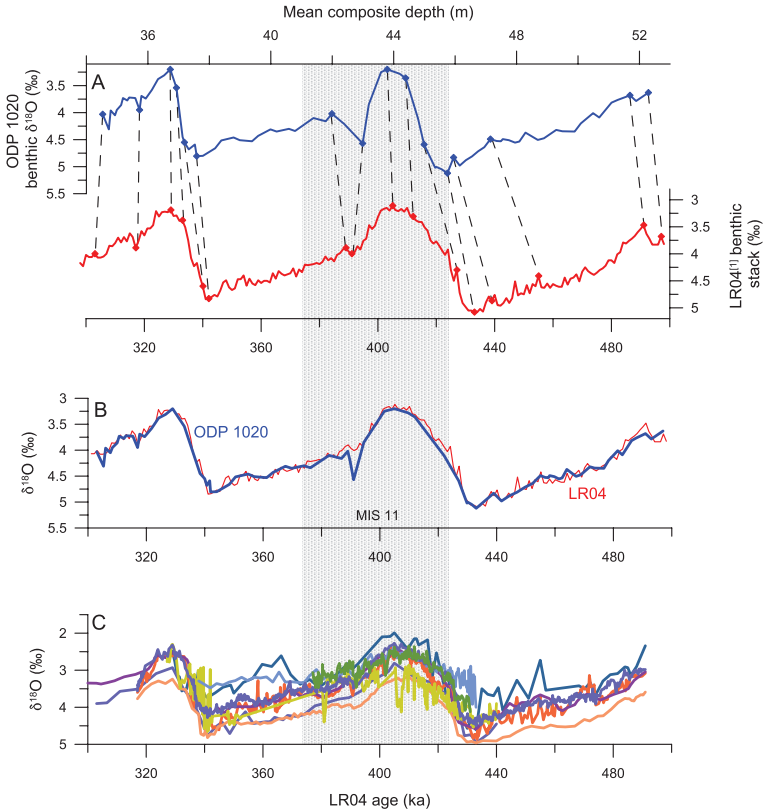

Fig. 2. Example for the age tuning of the benthic $\delta^{18}O$ record of ODP Hole 1020 to the benthic LR04 stack (Lisiecki and Raymo, 2005): **(A)** selection of age control points in the $\delta^{18}O$ of ODP 1020 and the LR04 stack, **(B)** comparison of the tuned $\delta^{18}O$ record of ODP Hole 1020 with the LR04 stack, and **(C)** nine benthic and planktonic oxygen isotope records from the North Atlantic used in this study tuned to the LR04 stack by the method as shown in panels **(A)** and **(B)**. The gray area indicates the MIS11 time interval according to Lisiecki and Raymo (2005).

CPD
9, 837–890, 2013

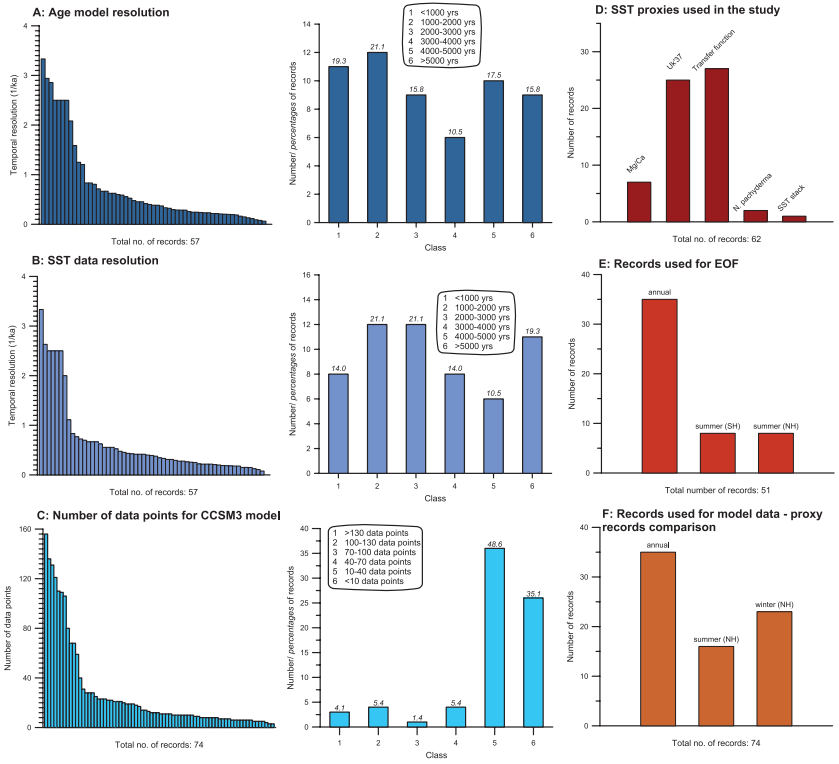

Fig. 3. Mean temporal resolution of the age models based on stable oxygen isotope records used in this study **(A)**. Mean temporal resolution of the SST records used in this study **(B)**. Number of available data points for the comparison of the proxy and model data temperature anomalies for the 390–420 ka time interval and number **(C)**. Number of SST records used in this study for each proxy **(D)**. Seasonal attribution of SST records used for the Empirical Orthogonal Function (EOF) analysis **(E)** and seasonal attribution of SST records used for the proxy-model data comparison **(F)**.

CPD
9, 837–890, 2013

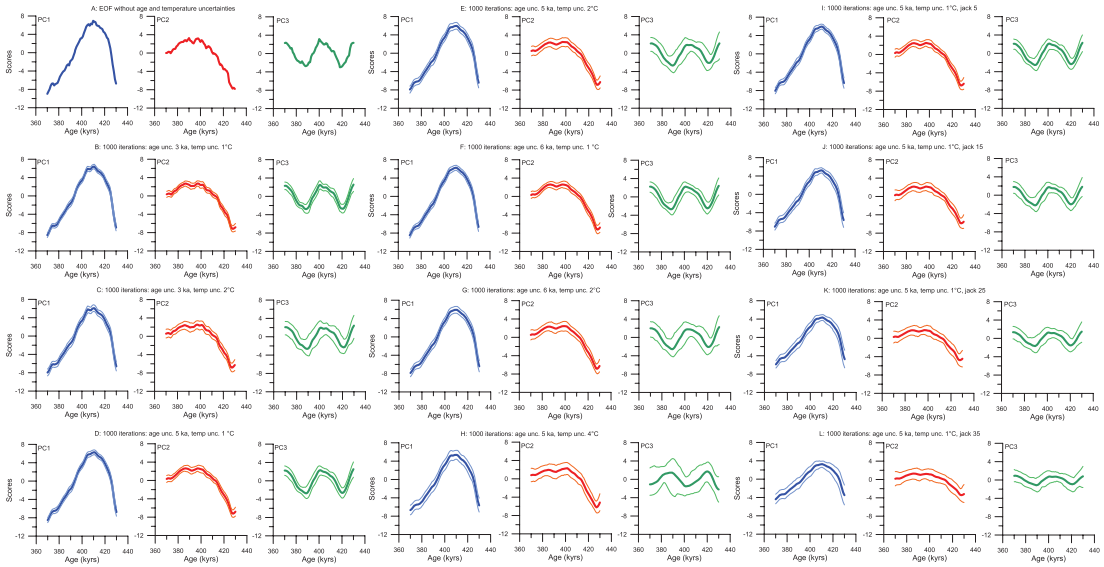

Fig. 4. Results of an Empirical Orthogonal Function (EOF) analysis of MIS11 SST records (Fig. 1, Table 1), including results of a sensitivity analysis with respect to age and temperature uncertainties. Re-calculations were made for age uncertainties of 3, 5 and 6 kyr, and for temperature uncertainties of 1, 2 and 4 °C **(A)**. To test for sensitivity of the EOF to record selection, jack-knifing was applied and 5, 15, 25 and 35 samples were randomly excluded from the data set (age and temperature uncertainties were set to 5 kyr and 1 °C) **(B)**. All calculations were made with 1000 iterations and the confidence intervals are given for each analysis. For variances explained by the EOFs see Table 3.

CPD
9, 837–890, 2013

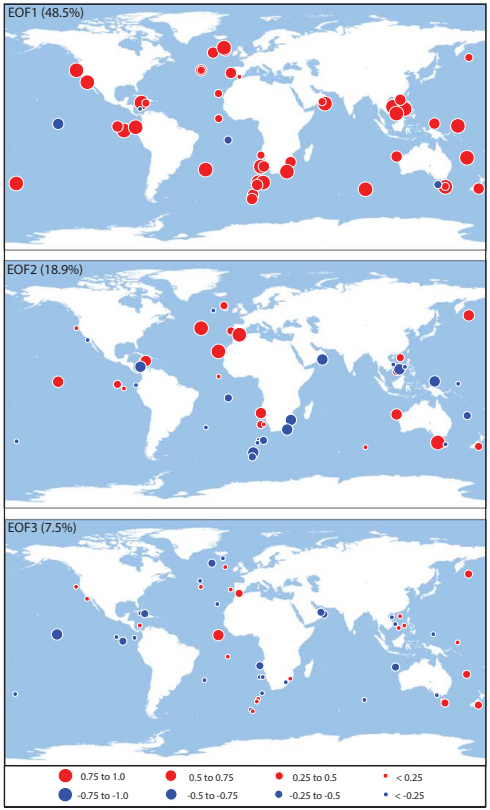

Fig. 5. Spatial distribution of the mean loadings of the first three EOF, based on 1000 iterations using an age and a temperature uncertainty of 5 kyr and 1 °C. Positive loadings are given in red, negative loadings are given in blue. Variance explained by each component is given in brackets. Almost all records show high positive loadings on the first EOF, while high positive loadings on the second EOF are restricted to the North Atlantic Ocean and the Mediterranean Sea, and south off Australia.

CPD
9, 837–890, 2013

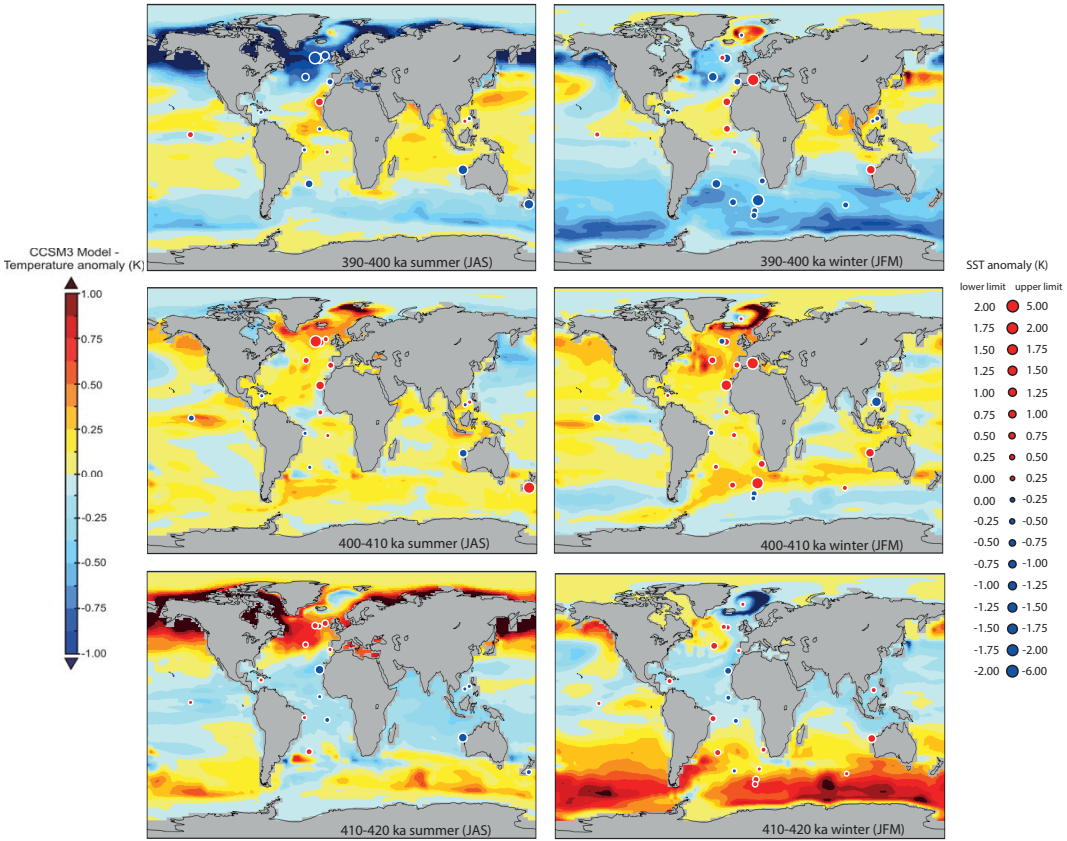

Fig. 6. A comparison of the boreal summer and winter sea surface temperature anomalies of proxy records with CCSM3 climate model results for 390–400, 400–410 and 410–420 ka time slices. Color and size scales indicate the magnitude of temperature anomalies relative to the mean SST of the three time slices.

CPD
9, 837–890, 2013

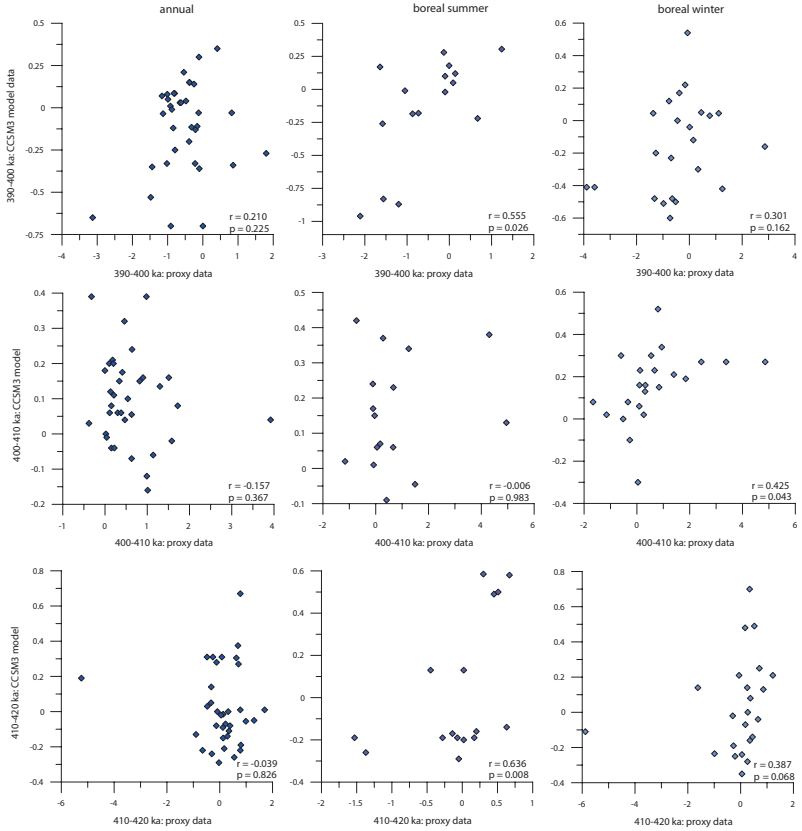

Fig. 7. Correlations between the proxy SST anomalies (annual, boreal summer and boreal winter) and the model SST anomalies for 390–400, 400–410 and 410–420 ka time slices. Given are the r-, ρ- and p-values (Table 4). Higher positive correlations between the proxy and model data can be observed for the boreal summer seasons of the 390–400 and 410–420 ka time slices and for the boreal winter season of the 400–410 ka time slice.

CPD
9, 837–890, 2013

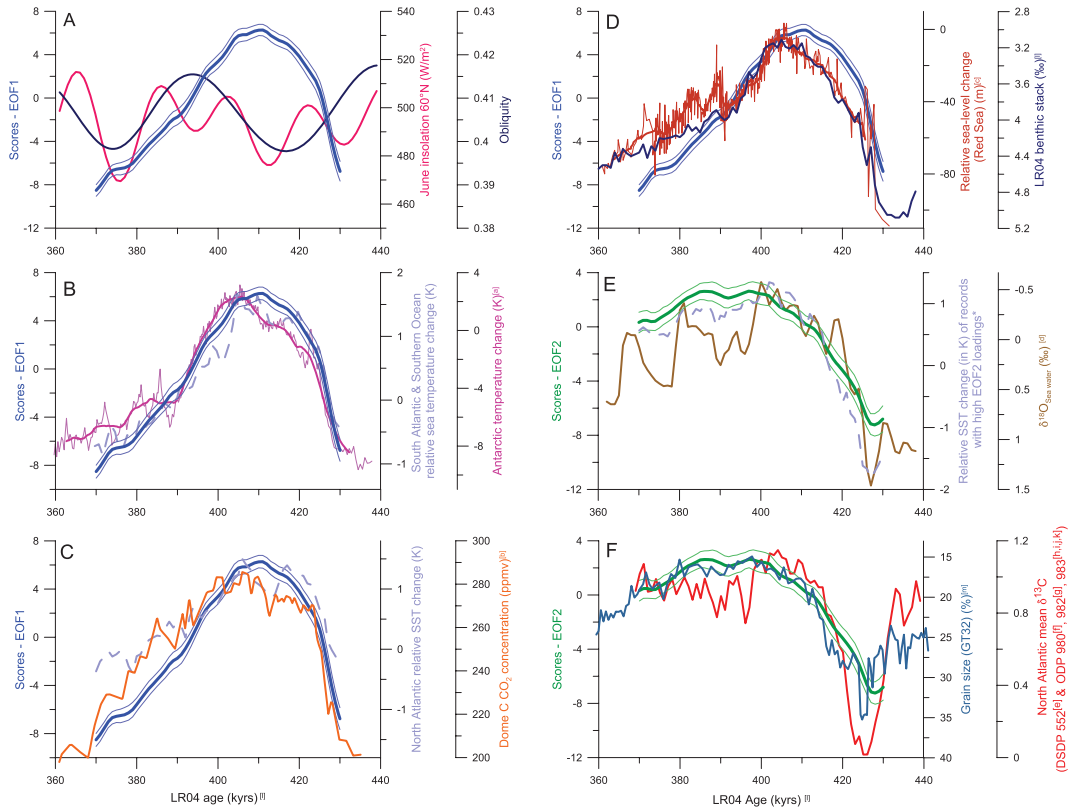

Fig. 8. Caption on next page.

CPD
9, 837–890, 2013

Global and regional sea surface temperature trends during MIS11

Y. Milker et al.

Fig. 8. Scores of the first EOF with their confidence intervals versus **(A)** orbital parameter (June insolation at 60° N and obliquity (Laskar et al., 2004), **(B)** relative temperature changes in the South Atlantic and Southern Ocean and Antarctic temperature changes recorded in the Dome C ice core during MIS11; Jouzel et al., 2007); [a]) (thin pink line: original data; thick pink line: smoothed curve), (C) mean relative temperature change in the North Atlantic records with high loadings to the first EOF and CO_2 concentration recorded in the Dome C ice core from the Antarctic (Siegenthaler et al., 2005; [b]), and **(D)** relative sea-level changes in the Red Sea (Rohling et al., 2009; [c]) and the LR04 benthic stack (Lisiecki and Raymo, 2005; [l]). Scores of the second EOF mean relative temperature changes in records with high positive loadings (>0.75) on the second EOF versus **(E)** δ^{18}O of sea water as proxy for ice volume (Elderfield et al., 2012; [d]), and **(F)** mean δ^{13}C values in the North Atlantic as a proxy for NADW strength and the East Asian winter monsoon signal as reflected by the GT32 grain size (content of >32 µm particles) in loess sequences (Hao et al. 2012; [m]; note inverse scale). For the mean of δ^{13}C North Atlantic records between 1100 and 2300 m water depth were selected according to according to Lisiecki et al. (2008). The δ^{13}C records used here are from Shackleton and Hall (1984) [e], Oppo et al. (1998) [f], Venz et al. (1999) [g], Raymo et al. (1998) [h], McIntyre et al. (1999) [i], Kleiven et al. (2003) [j], and Raymo et al. (2004) [k]. The EDC ages of the records from the Dome C ice core in **(B)** and **(C)** were converted into LR04 ages (Lisiecki and Raymo, 2005); [l]) according to Parrenin et al. (2007). * Records with high EOF2 loadings are from IODP U1313 & ODP 958 (North Atlantic), ODP 975 & ODP 976 (Mediterranean Sea) and ODP 1168 (south off Australia).

CPD
9, 837–890, 2013

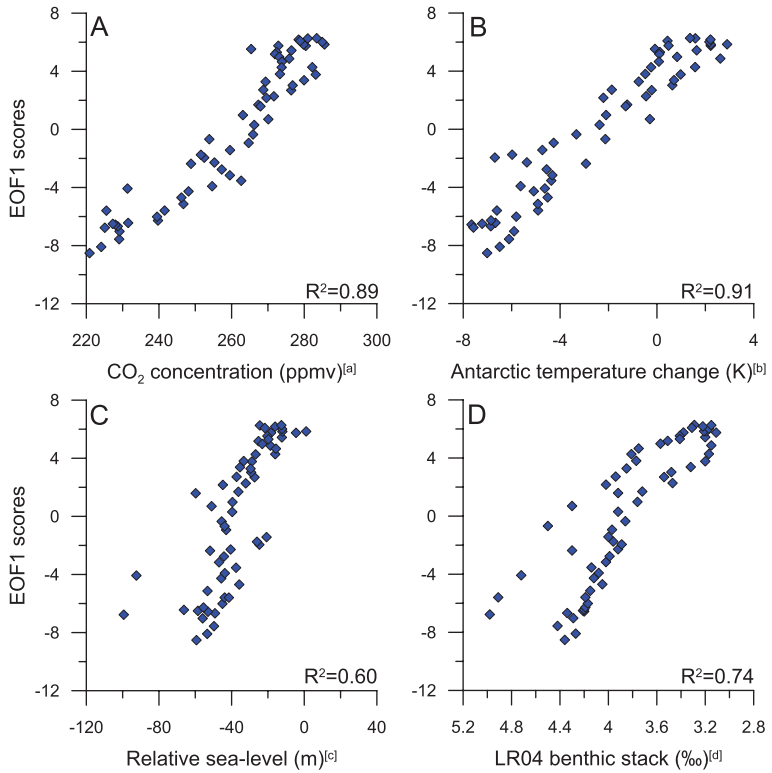

Fig. 9. Cross plots showing the correlation between EOF1 scores and **(A)** atmospheric CO_2 concentration (Siegenthaler et al., 2005), **(B)** Antarctic temperature change (Jouzel et al., 2007), **(C)** Red Sea relative sea level change (Rohling et al., 2009) and **(D)** the benthic LR04 stack (Lisiecki and Raymo, 2005). Most EOF runs (74–89 %) given here as numbers (*n*) show an earlier SST optimum than that recorded in Antarctica. EDC ages of the Antarctic temperature record were converted into LR04 ages according to Parrenin et al. (2007).

CPD
9, 837–890, 2013

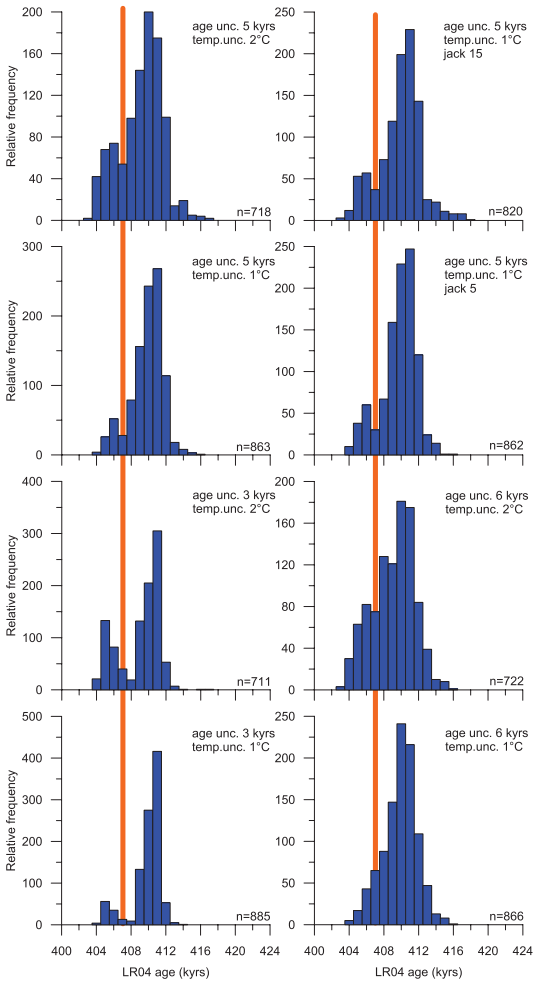

Fig. 10. Caption on next page.

CPD
9, 837–890, 2013

Fig. 10. Sea surface temperature optima during MIS11 calculated with various EOF analyses based on age and temperature uncertainties of 3–6 ka and 1–2 °C, respectively, and jackknifing versus temperature optimum observed in Antarctica (Jouzel et al., 2007) showing a lag of ~ 4 kyr between the SST optimum calculated with EOF1 and the Antarctic temperature optimum during MIS11. EDC ages of the Antarctic temperature record were converted into LR04 ages according to Parrenin et al. (2007).

CPD
9, 837–890, 2013

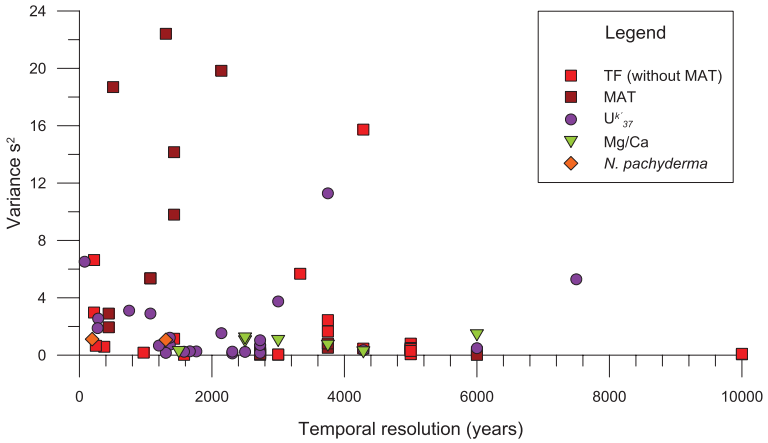

Fig. 11. Variances of the proxy SST records versus their temporal resolution. High variances in the SSTs are found in low resolution records particularly estimated with the Modern Analog Technique while most of the other records showing lower variances with higher resolution.

CPD
9, 837–890, 2013